ORNL-6703

ornl

OAK RIDGE NATIONAL LABORATORY

MARTIN MARIETTA

Multifracture of Ceramic Composites

Y. J. Weitsman
H. Zhu

MANAGED BY
MARTIN MARIETTA ENERGY SYSTEMS, INC.
FOR THE UNITED STATES
DEPARTMENT OF ENERGY

ORNL--6703

DE92 009630

Engineering Technology Division

MULTIFRACTURE OF CERAMIC COMPOSITES

Y. J. Weitsman
Oak Ridge National Laboratory/
The University of Tennessee at Knoxville

H. Zhu
The University of Tennessee at Knoxville

DATE PUBLISHED: MARCH 1992

Prepared by the
OAK RIDGE NATIONAL LABORATORY
Oak Ridge, Tennessee 37831-6285
managed by
MARTIN MARIETTA ENERGY SYSTEMS, INC.
for the
U.S. DEPARTMENT OF ENERGY
under contract DE-AC05-84OR21400

CONTENTS

LIST OF FIGURES

NOMENCLATURE

a	radius of fiber
A, B, C	constants associated with various displacements
b	radius of representative volume element
E	Young modulus
$f(z), g(z), k(z), F(z)$	shape functions of the coordinate z
G	shear modulus
i, j	displacement stress and strain indices
L	matrix crack spacing
l_S	length of slip zone along fiber/matrix interface
P, Q, S	integrated values of p, q, and s
$p, q, s, \hat{p}, \hat{q}, t$	shape functions of the coordinate r
P_f	probability of fiber failure
r, θ, z	cylindrical coordinates
T	thermal excursion temperature
u	radial displacement
U	energy
V	volume fraction
w	axial displacement
x,y	Cartesian coordinates
z_{fb}	location of fiber break
α	coefficient of thermal expansion
Δw	displacement discontinuity at fiber/matrix interface
ε	strain
ε_0	average axial strain in test sample
λ	Lagrange multiplier
Π, Π^*, π_1, π_2	energy functionals
σ	normal stress
σ_a	average applied axial stress
σ_0, M	Weibull distribution parameters
τ	shear stress
τ_s	maximal shear stress supported by fiber/matrix interface
υ	Poisson's ratio
$\mathcal{G}_m^c$	critical energy release rate for matrix fracture

SUBSCRIPTS

f	fiber
m	matrix

MULTIFRACTURE OF CERAMIC COMPOSITES

Y. J. Weitsman*
H. Zhu†

ABSTRACT

This work presents a mechanistic model for the multifracture process of uniaxially reinforced fibrous ceramic composites under monotonically increasing tension parallel to the fiber direction. The model employs an energy criterion to account for the progression of matrix cracks, bridged by intact fibers, and Weibull failure statistics to relate the failure of the fibers. Consideration is given to the interactions between the foregoing failure processes as well as to the effects of various material parameters on the response of the composite.

---

1. INTRODUCTION

Ceramic materials exhibit superior performance at high temperatures, but their utilization in critical structural components is severely curtailed by their excessive brittleness. Techniques to alleviate this brittleness are the subject of intensive research, reviewed by several leading investigators in the field (e.g., Schioler and Stiglich 1986, Hillig 1987, and Evans 1990). In one such technique, continuous fiber-reinforced ceramic composites (CFCC) are formed; in these composites, the reinforcing ceramic fibers are typically more ductile than the ceramic matrix. In this case, fracture of the brittle matrix entangles the more compliant fibers in the failure process, resulting in several energy-consuming mechanisms. If appropriately conceived, these mechanisms lead to a gradual structural failure instead of catastrophic collapse.

Typical stress-strain curves are shown in Figs. 1.1 and 1.2. Figure 1.1 exhibits the ductile behavior of unidirectionally reinforced SiC/CAS ceramics under uniaxial tension parallel to the fiber direction, with comparison to results obtained by Daniel, Anastassopoulus, and Lee (1989). Figure 1.2, obtained by Nardone and Prewo (1988), shows similar results for HMU-7740 composites, with a significant reversal in the lateral strain.

Several striking differences exist between ceramic and, say, polymeric composites. In polymeric composites, the fibers provide stiffness, while the polymer serves essentially as a binder. Consequently, the ratio E_f/E_m of the fiber and polymer moduli is typically of $O(10^2)$. In addition, to achieve high stiffness it is usually desirable to have strong interfacial bonding

---

*Oak Ridge National Laboratory/The University of Tennessee, Knoxville, Distinguished Scientist in Composite Materials and Structures.

†Postdoctoral Research Fellow, The University of Tennessee, Knoxville.

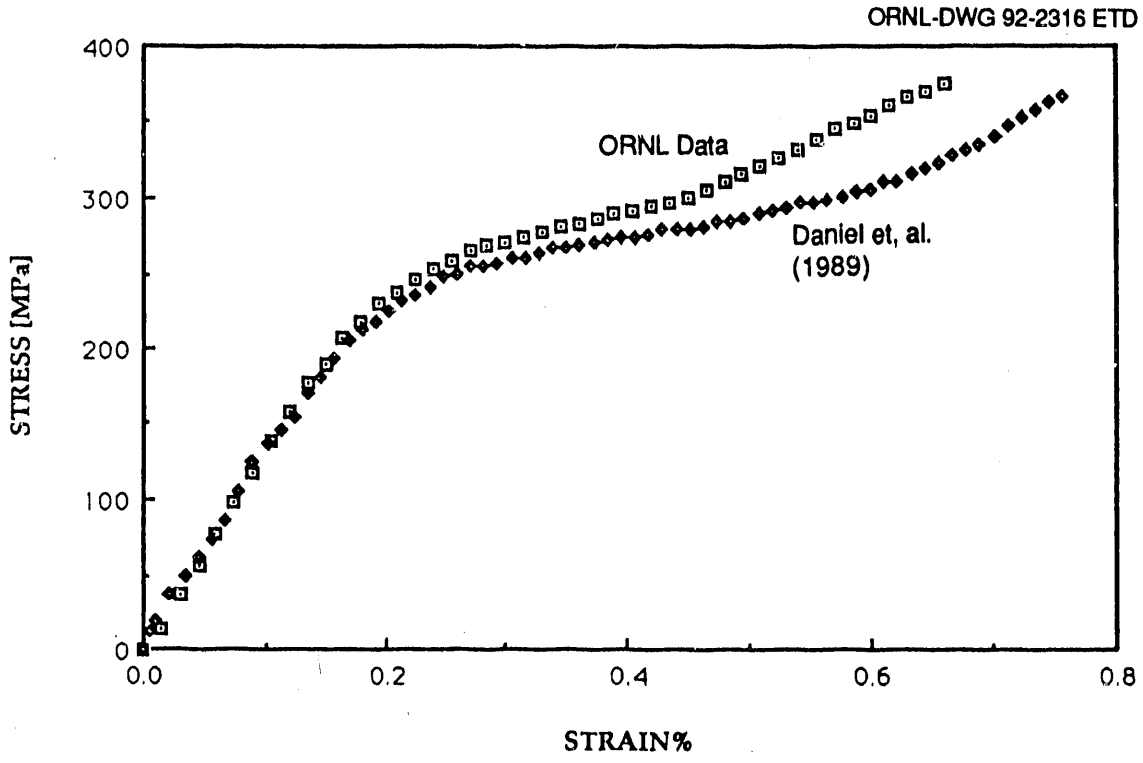

Fig. 1.1. The uniaxial stress-strain response of 0° SiC/CAS continuous fiber-reinforced ceramic composites.

between the fiber and matrix materials. In contrast, the primary role of the fibers in ceramic composites is to enhance toughness. Thus, the ratio E_f/E_m in ceramic composites is typically of O(1). Moreover, it is usually desirable to have weak bonding between the fibers and matrix to enhance interfacial slip, thereby increasing the amount of energy dissipation during the process of matrix cracking. In addition, a weak interfacial bond will deflect matrix cracks around the fibers and bring into play their larger ductility. Therefore, in spite of some similarities, the modelling and analysis of failure of ceramic composites require a different approach than that applied to polymeric composites. Among the several ceramic failure models worth mentioning, we recall those of Aveston, Cooper, and Kelly (1971) and Budiansky, Hutchinson, and Evans (1986). Both works model the fracture behavior of a brittle matrix reinforced by ductile fibers. The former employs a stress criterion for failure, while the latter utilizes energy criteria. Both analyses aim at predicting the onset of the first matrix crack, and both approaches are based upon the shear-lag model.

The latter model assumes that the fibers carry all the tensile load and that the matrix responds in shear only. In addition, the model neglects all shear deformation within the fibers. However, the above assumptions, which are reasonably accurate for E_f/E_m ratios of $O(10^2)$ as occur in polymeric composites, appear to be deficient in the case of ceramics. It is intuitively obvious that for E_f/E_m of O(1), the shears in the fibers and the matrix play equally important roles and that, equivalently, the normal stresses in the matrix should not be neglected. In addition, the normal stresses in the fibers in the vicinity of the matrix crack are expected to

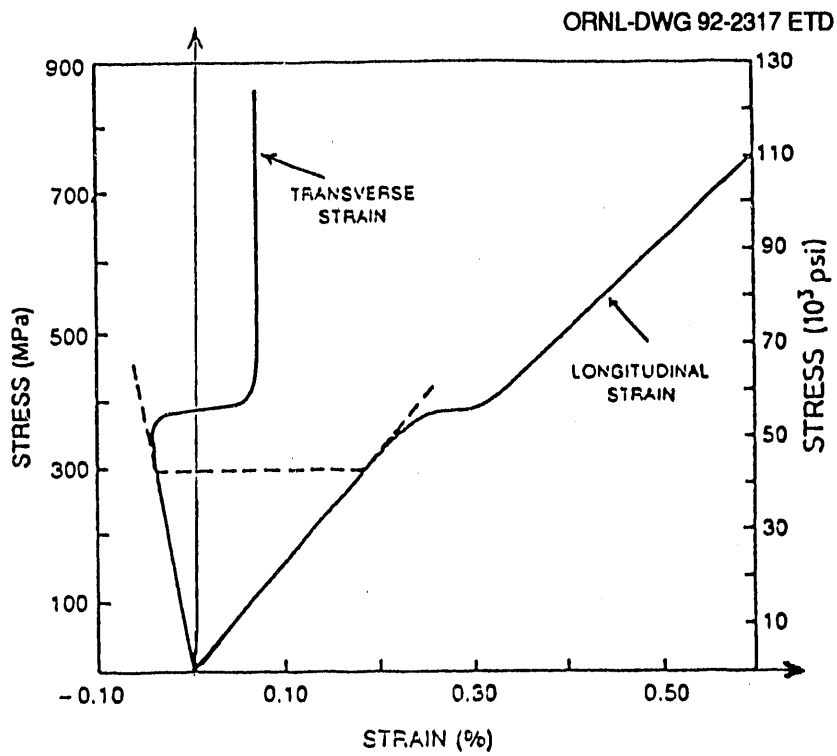

Fig. 1.2. Longitudinal and transverse strain against applied tensile load for 0°, 43 vol % HMU-7740 composites. *Source*: V. C. Nardone and K. M. Prewo, 1988, "Tensile Performance of Carbon-Fibre-Reinforced Glass," *J. Mater. Sci.*, 23, 168–180.

exhibit a very pronounced radial variation that plays a critical role in the prediction of fiber failure. The importance of the foregoing stress distribution was alluded to by several investigators (Sutcu 1989, Schwietert and Steif 1990), although they did not quantify or analyze it. Finally, the evolution of multiple cracks within CFCC has not been modelled in the context of energy considerations. A major obstacle in evaluating the energies consumed during the process of progressive failure in CFCC can be traced to yet another inadequacy of the shear-lag model, namely, its limited ability to express the interfacial slip between fibers and matrix and its attendant incapacity to evaluate the dissipative energy.

Energy-based analyses of the multifracture behavior of laminated polymeric composites, when progressive failure occurs at the ply level, were developed by Fang, Schapery, and Weitsman (1986) and by Nuismer and Tan (1988). The latter work employs concepts of shear-lag.

An important improvement in the analytical representation of mechanical fields associated with a single matrix crack around a relatively ductile fiber was obtained by McCartney (1989). That representation satisfied most of the field equations and boundary conditions required by an exact solution. Nevertheless, in the present work it was found advantageous to establish another representation more suitable to our purpose of analyzing the interactive effects between fiber failures and the multifracturing process within the matrix. In particular, our representation contains specific details of the stress distribution $\sigma_z^f(r, z)$ within the fibers, which are

predicting the ensuing fiber failure process. This aspect seems to be of particular importance because fiber flaws appear to occur more readily near the outer surface of the fiber, thereby corresponding to a Weibull statistical representation that employs surface rather than volume integrals. It turns out that statistical computations employing average values $\bar{\sigma}_z^f(z)$ predict substantially lower failure probabilities than computations based on the stresses at the interface $r = a$, namely $\sigma_z^f(a, z)$.

The present formulation assumes that the slip process is caused by relative movement over asperities at the fiber/matrix interfaces. Other considerations, such as Coulomb friction, are obviously possible. These were considered by Dollar and Steif (1988), Steif and Dollar (1988), and, in a broader context, by Hutchinson and Jentsen (1990).

2. FORMULATION OF THE APPROXIMATE MECHANICS SOLUTION

Consider a unidirectionally reinforced composite material, consisting of ceramic fibers and a ceramic matrix, subjected to uniaxial tension parallel to the fiber direction. Beyond a certain level of applied stress, the composite is assumed to develop matrix cracks in planes normal to the fiber direction. These cracks are bridged by intact fibers and are spaced at an average distance L. In addition, the composite is assumed to be cooled down by T degrees below its stress-free temperature T_0.

Let r, θ, and z denote cylindrical coordinates, with corresponding displacements u, v, and w, respectively; designate stresses by the standard symbols, σ_r, σ_z, τ_{rz}, etc. In addition, let m and f denote matrix and fiber properties, respectively.

The thermomechanical problem at hand will be formulated for the representative volume element (RVE) shown in Fig. 2.1. The RVE occupies the volume $0 \le r \le b$, $-L/2 < z < L/2$, and contains two concentric cylinders. The fiber region is located within $0 \le r < a$, $|z| \le L/2$, and the matrix domain ranges over $a < r \le b$, $|z| < L/2$. Matrix cracks are supposed to pre-exist at $z = \pm L/2$, and the interfacial shear stress $\tau_{rz}(a,z)$ is assumed to be limited by a slip stress of magnitude τ_s. At $\tau_{rz}(a,z) = \tau_s$, relative displacement Δw_s (slip) is supposed to occur by an amount of $\Delta w_s = w_m(a,z) - w_f(a,z)$, which is yet to be determined. The slip mechanism is assumed to occur as relative motion over interfacial asperities at $r = a$.

We assume that both fiber and matrix materials behave linearly elastic and that their interfaces remain in lateral contact even in the presence of tangential slip. The maintenance of lateral contact is intuitively justified for materials systems where $\alpha_m > \alpha_f$ and $\nu_m > \nu_f$, where α and ν denote the coefficient of thermal expansion and Poisson's ratio, respectively, and when slip occurs over interfacial asperities of sufficiently large amplitudes.

The boundary value problem for the RVE consists of the linear, isotropic, elastic field equations within the fiber and matrix regions. Employing standard notation, these equations read

$$\varepsilon_{ij}^{f,m} = \frac{1}{E_{f,m}}\left[\left(1+\nu_{f,m}\right)\sigma_{ij}^{f,m} - \nu_{f,m}\sigma_{kk}^{f,m}\delta_{ij}\right] + \alpha_{f,m}T\delta_{ij} \quad , \tag{1}$$

where

$$2\varepsilon_{ij}^{f,m} = u_{i,j}^{f,m} + u_{j,i}^{f,m} \quad . \tag{2}$$

Assuming rotational symmetry, we have $v = 0$, $\varepsilon_{r\theta} = \varepsilon_{z\theta} = \sigma_{r\theta} = \sigma_{z\theta} = 0$, whereby the equilibrium equations read

$$\frac{\partial \sigma_z^{f,m}}{\partial z} + \frac{\partial \tau_{rz}^{f,m}}{\partial r} + \frac{\tau_{rz}^{f,m}}{r} = 0 \quad , \tag{3a}$$

$$\frac{\sigma_r^{f,m} - \sigma_\theta^{f,m}}{r} + \frac{\partial \sigma_r^{f,m}}{\partial r} + \frac{\partial \tau_{rz}^{f,m}}{\partial z} = 0 \quad . \tag{3b}$$

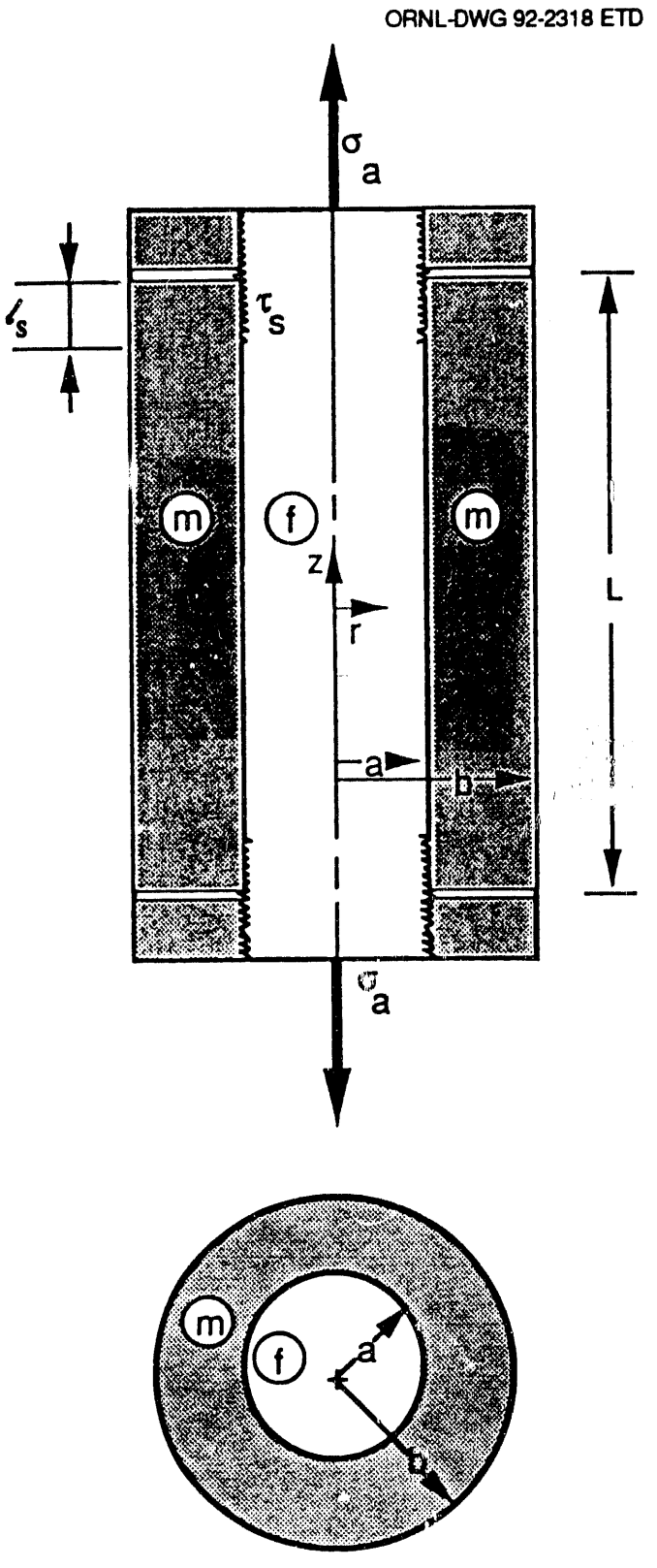

Fig. 2.1. The representative volume element.

An exact elasticity solution satisfies the following boundary conditions for the RVE:

$$\left.\begin{aligned} \sigma_r^m(b,z) &= 0 \\ \tau_{rz}^m(b,z) &= 0 \end{aligned}\right\} \quad |z| \le \frac{L}{2} \tag{4a,b}$$

$$\left.\begin{aligned} \sigma_r^m(a,z) &= \sigma_r^f(a,z) \\ \tau_{rz}^m(a,z) &= \tau_{rz}^f(a,z) \\ u_m(a,z) &= u_f(a,z) \end{aligned}\right\} \quad |z| \le \frac{L}{2} \tag{5a,b,c}$$

and

$$w_m(a,z) = w_f(a,z) \tag{6a}$$

within the contact region (say $|z| \le L/2 - l_s$),

$$\left|\tau_{rz}^m(a,z)\right| = \left|\tau_{rz}^f(a,z)\right| = \tau_s \tag{6b}$$

within the slip zone (say $L/2 - l_s \le |z| \le L/2$).

In addition, the condition of "global" equilibrium gives

$$2\pi \int_0^a \sigma_z^f r\, dr + 2\pi \int_a^b \sigma_z^m r\, dr = \pi b^2 \sigma_a \quad , \tag{7}$$

where $\sigma_a = \overline{\sigma}_z$ is the average value of the applied stress.

The presence of matrix cracks at $z = \pm L/2$ implies

$$\left.\begin{aligned} \sigma_z^m\left(r, \pm\frac{L}{2}\right) &= 0 \\ \tau_{rz}^m\left(r, \pm\frac{L}{2}\right) &= 0 \end{aligned}\right\} \quad a < r \le b \ . \tag{8a,b}$$

Finally, the planes $z = \pm L/2$ may be viewed as symmetry planes for cylindrical RVEs stacked vertically along the z-axis. Therefore,

$$w_f\left(r, \frac{L}{2}\right) = C_1 \quad \text{and} \quad w_f\left(r, \frac{L}{2}\right) = C_2 \ , \quad 0 \le r < a \tag{9}$$

and

$$\tau_{rz}^f\left(r, \pm\frac{L}{2}\right) = 0 \qquad 0 \le r < a \ . \tag{10}$$

In the sequel, an approximate solution to the foregoing boundary value problem will be developed by means of an "enhanced" kinematically admissible field. This field will provide displacements u_f, u_m, w_f, and w_m that satisfy all the kinematic conditions of our problem, namely, Eqs. (5c), (6a), and (9).

The paramount stresses in the present problem are $\sigma_z^{f,m}$ and $\tau_{rz}^{f,m}$, associated primarily with the displacements $w_{f,m}$ and their spatial derivatives. The in-plane stresses $\sigma_r^{f,m}$ and $\sigma_\theta^{f,m}$ are mainly due to the lateral contractions $\varepsilon_r^{f,m}$ and $\varepsilon_\theta^{f,m}$, associated with the displacements $u_{f,m}$. Their effect on $\sigma_z^{f,m}$ are of $O(\nu^2)$, where $\nu \sim \nu_m \sim \nu_f$ (see Appendix A).

Guided by these observations, we shall construct "enhanced" kinematically admissible fields for $u_{f,m}$ disparately from those for $w_{f,m}$. Specifically, we shall initially consider an uncracked RVE with $u_f(r)$ and $u_m(r)$ and assume $w_f = w_m = \varepsilon_0 z$ [instead of a cracked RVE with $w_f(r, z)$ and $w_m(r, z)$]. For these displacements, we shall employ Eqs. (1) and (2) to generate stresses $\sigma_r^{f,m}$ and $\sigma_\theta^{f,m}$, which satisfy Eqs. (3b), (4a), (5b), as well as—obviously—(5c). Note that, with the foregoing choice of displacements, $\tau_{rz}^f = \tau_{rz}^m = 0$. As shown in Appendix A, the uniform strain $\varepsilon_z = \varepsilon_0$ is related to the applied stress σ_a and to T. In the presence of matrix cracks, we shall employ an iterative procedure to improve the above-mentioned approximation by adjusting the value of ε_0 to correspond to an appropriately modified equivalent modulus. The modification will be updated with increasing crack density. We subsequently consider $w_f = w_f(r, z)$ and $w_m = w_m(r, z)$ and substitute the already available expressions for $\sigma_r^{f,m}$ and $\sigma_\theta^{f,m}$ in Eqs. (1) and (2) to relate $\sigma_z^{f,m}$ to $\partial w_{f,m}/\partial z$. Then, shear stresses $\tau_{rz}^{f,m}$ that satisfy Eq. (3a) with conditions (4b), (5b), and (6b) are evaluated. For kinematic admissibility, the condition (6a) must of course be satisfied. In addition, we shall also fulfill conditions (7), (8a), and (9).

Clearly, the above kinematically admissible fields $u_f(r)$, $u_m(r)$, $w_f(r, z)$, and $w_m(r, z)$ do not provide the exact solution to the boundary value problem stated in Eqs. (1) through (10). The major inadequacy resides in the evaluation of τ_{rz}. The shear stresses $\tau_{rz}^{f,m}$ derived from the equilibrium equation (3a) are inconsistent with expressions deduced from the stress-strain relations (1) and contradict the premise that $\tau_{rz}^{f,m} = 0$, which was utilized in the approximate construction of the displacements $u_f(r)$ and $u_m(r)$. Furthermore, these shear stresses do not satisfy the boundary conditions (8b) and (10). These shortcomings are not surprising because an approximate solution cannot handle the extremely intricate corner singularity that, under perfect interfacial contact, occurs along the circle $r = a$, $z = L/2$, where the symmetry of the stress tensor no longer holds and $\tau_{zr} \neq \tau_{rz}$ (Bogy 1968).* On the other hand, the inadequacy of our solution is mitigated by the fact that the approximation is optimized through the use of a minimum potential energy principle and guided by a numerical solution to a simpler, but closely related, problem.

*However, this singularity may be eliminated when a crack impinges on a frictional interface (e.g., Dollar and Steif 1989).

3. THE KINEMATICALLY ADMISSIBLE DISPLACEMENT FIELD

3.1 PERFECTLY BONDED INTERFACES (NO SLIP)

It is well known (e.g., Timoshenko and Goodier 1951) that the following radial displacements

$$u_f = Ar \ , \qquad u_m = Ar + B\left(r - \frac{a^2}{r}\right) \ , \tag{11}$$

together with $w_f = w_m = \varepsilon_0 z$, generate stresses according to Eq. (1) that satisfy the equilibrium equation (3b). In the sequel, expressions (11) represent the kinematically admissible displacements u_m and u_f.

Turning to the displacements w_f and w_m, introduce first the shape functions $p(r)$, $q(r)$, and $s(r)$ with the following stipulations: $p(0) = q(a) = 0$, $p(a) = q(0) = s(a) = 1$. In addition, denote

$$P = \frac{2}{a^2}\int_0^a rp(r)dr \ , \quad Q = \frac{2}{a^2}\int_0^a rq(r)dr \ , \quad S = \frac{2}{b^2 - a^2}\int_a^b rs(r)dr \ .$$

Assume the following forms for the strains ε_z:

$$\varepsilon_z^f = p(r)[f(z) + C] + q(r)g(z) \ , \qquad \varepsilon_z^m = s(r)f(z) + C \ . \tag{12}$$

These strains will generate displacements $w_{f,m} = \int_0^z \varepsilon_z^{f,m}(\hat{z}, r)d\hat{z}$, which are continuous at the interface $r = a$ for all continuous functions $f(z)$ and $g(z)$ and for any arbitrary constant C.

In view of Eqs. (1), (11), and (12), we have

$$\sigma_z^f = \frac{E_f(1-\nu_f)\{p(r)[f(z)+C]+q(r)g(z)\}}{(1+\nu_f)(1-2\nu_f)} + \frac{2E_f\nu_f A}{(1+\nu_f)(1-2\nu_f)} - \frac{E_f}{1-2\nu_f}\alpha_f T \tag{13a}$$

and

$$\sigma_z^m(r,z) = \frac{E_m(1-\nu_m)[s(r)f(z)+C]}{(1+\nu_m)(1-2\nu_m)} + \frac{2E_m\nu_m(A+B)}{(1+\nu_m)(1-2\nu_m)} - \frac{E_m}{1-2\nu_m}\alpha_m T \ . \tag{13b}$$

To satisfy boundary condition (8a), the form of Eq. (13b) must be modified to read

$$\sigma_z^m(r,z) \sim s(r)f(z) \quad \text{with} \quad f\left(\pm\frac{L}{2}\right) = 0 \ .$$

Consequently, we have

$$C = \frac{1+\nu_m}{1-\nu_m}\alpha_m T - \frac{2\nu_m(A+B)}{1-\nu_m}$$

and

$$\sigma_z^m(r,z)=\frac{E_m(1-\nu_m)s(r)f(z)}{(1+\nu_m)(1-2\nu_m)} \quad .$$

Denote now

$$E_f^*=\frac{E_f(1-\nu_f)}{(1+\nu_f)(1-2\nu_f)} \quad , \quad E_m^*=\frac{E_m(1-\nu_m)}{(1+\nu_m)(1-2\nu_m)} \quad ,$$

and

$$\sigma_0=V_fE_f^*\left(CP-\frac{1+\nu_f}{1-\nu_f}\alpha_fT+\frac{2\nu_fA}{1-\nu_f}\right) \quad ,$$

with the volume fractions $V_f = a^2/b^2$ and $V_m = (b^2 - a^2)/b^2$. Employing Eq. (7), the force balance in the z-direction gives

$$\sigma_a = V_fE_f^*[Pf(z) + Qg(z)] + V_mE_m^*Sf(z) + \sigma_0 \quad , \tag{14}$$

whereby $g(z)$ can be expressed in terms of $f(z)$ as follows

$$g(z)=\left[\frac{\sigma_a-\sigma_0}{V_fE_f^*}-Pf(z)-\frac{V_mE_m^*}{V_fE_f^*}Sf(z)\right]\Big/Q \quad . \tag{15}$$

Substituting expression (15) in Eqs. (12) and (13a) yields

$$\sigma_z^f = E_f^*f(z)\left[p(r)-\frac{q(r)}{Q}\left(P+S\frac{V_mE_m^*}{V_fE_f^*}\right)\right]+E_f^*C[p(r)-P]+\frac{\sigma_0}{V_f}\left[1-\frac{q(r)}{Q}\right]+\frac{\sigma_aq(r)}{V_fQ} \quad , \tag{16a}$$

$$\varepsilon_z^f = f(z)\left[p(r)-\frac{q(r)}{Q}\left(P+S\frac{V_mE_m^*}{V_fE_f^*}\right)\right]+p(r)C+\frac{(\sigma_a-\sigma_0)q(r)}{QV_fE_f^*} \quad . \tag{16b}$$

The latter equation gives

$$w_f = F(z)\left[p(r)-\frac{q(r)}{Q}\left(P+S\frac{V_mE_m^*}{V_fE_f^*}\right)\right]+p(r)Cz+\frac{(\sigma_a-\sigma_0)q(r)z}{QV_fE_f^*} \quad . \tag{16c}$$

Employing the equilibrium equation (3a) to determine the shear stress, we have

$$\tau_{rz}^f=-\frac{1}{r}\int_0^r r^*\frac{\partial\sigma_z^f}{\partial z}dr^*=-\frac{E_f^*f'(z)}{r}\int_0^r\left[p(r^*)-\frac{q(r^*)}{Q}\left(P+S\frac{V_mE_m^*}{V_fE_f^*}\right)\right]r^*dr^* \quad . \tag{16d}$$

As noted earlier, the result (16d) is inconsistent with the outcome derived from the stress-strain relations (1).

Turning to the matrix region $a \le r \le b$, $|z| < L/2$ we obtain

$$\sigma_z^m = E_m^*f(z)s(r) \quad , \tag{17a}$$

$$\varepsilon_z^m = s(r)f(z)+C \quad , \tag{17b}$$

$$w_m = s(r)F(z)+Cz \quad , \tag{17c}$$

and

$$\tau_{rz}^m = -\frac{1}{r}\int_0^a r^*\frac{\partial\sigma_z^f}{\partial z}dr^* - \frac{1}{r}\int_a^r r^*\frac{\partial\sigma_z^m}{\partial z}dr^*$$

$$= \frac{f'(z)E_m^*}{r}\left[0.5a^2S\frac{V_m}{V_f} - \int_a^r s(r^*)r^*dr^*\right] . \tag{18}$$

In Eqs. (16c) and (17c), we denoted $F(z) = \int_0^z f(z^*)dz^*$.

3.2 AN INTERFACIAL SLIP ZONE UNDER CONSTANT SHEAR STRESS

It is assumed that the absolute value of the interfacial shear stress $|\tau_i(z)| = |\tau_{rz}(a,z)|$ cannot exceed the limiting value of τ_s and that interfacial slip in the amount of $\Delta w(z) = w_m(a,z) - w_f(a,z)$ occurs when $\tau_i(z) = \pm\tau_s$. The direction of Δw coincides with the sign of τ_i. In this circumstance, boundary condition (6b) replaces the displacement continuity condition (6a).

To focus ideas, assume slip to occur at the cylindrical interface $r = a$, $L/2 - l_s < z \le L/2$. In this case, we confine the range of applicability of the foregoing expressions for perfectly bonded interfaces to the region $0 \le z \le L/2 - l_s$ (instead of $0 \le z \le L/2$) and construct a "slip zone solution" for the region $0 \le r \le b$, $L/2 - l_s < z \le L/2$.

The "slip zone formulation" will satisfy the same field equations and boundary conditions as the foregoing formulation for perfectly bonded interfaces, except that Eq. (6b) replaces Eq. (6a). In addition, the two formulations must blend together to ascertain continuity of tractions and displacements at $z = L/2 - l_s$, namely, continuity of u_m, u_f, w_m, w_f, σ_r^m, σ_z^f, and τ_{rz}^m, τ_{rz}^f at $z = L/2 - l_s$.

In view of Eqs. (3a) and (6b), we now have

$$\tau_{rz}^f(a,z) = -\frac{1}{a}\int_0^a r\frac{\partial\sigma_z^f}{\partial z}dr = -\tau_s = \tau_{rz}^m(a,z) \quad , \quad \frac{L}{2} - l_s < z \le \frac{L}{2} \quad . \tag{19}$$

Guided by Eq. (19), we select

$$\sigma_z^f = \left(\frac{L}{2} - z\right)\hat{p}(r) + \hat{q}(r) + H(r,z) \tag{20a}$$

and

$$\sigma_z^m = \left(\frac{L}{2} - z\right)\hat{s}(r) \quad , \tag{20b}$$

with the following provisos:

$$\frac{1}{a}\int_0^a r\hat{p}(r)dr = \tau_s \quad , \tag{21a}$$

$$\int_0^a r\,\frac{\partial H(r,z)}{\partial z}\,dr = 0 \quad , \tag{21b}$$

$$\int_0^a r\hat{p}(r)dr + \int_a^b r\hat{s}(r)\,dr = 0 \quad , \tag{21c}$$

$$\int_0^a r\hat{q}(r)dr = \sigma_a\,\frac{b^2}{2} \quad , \tag{21d}$$

$$\int_0^a rH(r,z)dr = 0 \quad . \tag{21e}$$

Conditions (21a) and (21b) satisfy Eq. (19), condition (21c) gives $\tau_{rz}^m(b,z) = 0$, and conditions (21d) and (21e) with (21c) satisfy Eq. (7).

Conditions (21b) and (21e) can be satisfied simultaneously by selecting $H(r,z) = t(r)k(z)$, with $k(z) = (z - L/2 + l_s)^2$ and $\int_0^a rt(r)dr = 0$. The foregoing choice of $k(z)$ also facilitates the establishment of traction and displacement continuity at $z = L/2 - l_s$. Traction continuity at $z = L/2 - l_s$ between the expressions listed in Eqs. (16a), (16d), (17a), and (18) that are consistent with the forms proposed in Eq. (20) can now be established in a straightforward manner. We obtain

$$\sigma_z^f = \frac{2\tau_s V_f E_f^*}{aSV_m E_m^*}\left(\frac{L}{2} - z\right)\left[p(r) - \frac{q(r)}{Q}\left(P + S\frac{V_m E_m^*}{V_f E_f^*}\right)\right] + E_f^* C[p(r) - P]$$
$$+ \frac{\sigma_0}{V_f}\left[1 - \frac{q(r)}{Q}\right] + \frac{\sigma_a q(r)}{V_f Q} + t(r)k(z) \quad , \tag{22a}$$

$$\sigma_z^m = s(r)\,\frac{2\tau_s V_f}{aSV_m}\left(\frac{L}{2} - z\right) \quad , \tag{22b}$$

and

$$\tau_{rz}^f = \frac{2\tau_s V_f E_f^*}{aSV_m E_m^* r}\int_0^r \left[p(r^*) - \frac{q(r^*)}{Q}\left(P + S\frac{E_m^* V_m}{E_f^* V_f}\right)\right] r^* dr^*$$
$$- \frac{2(z - L/2 + l_s)}{r}\int_0^r t(r^*)r^* dr^* \tag{22c}$$

$$\tau_{rz}^m = -\frac{2\tau_s}{aSr}\left[\frac{a^2 S}{2} - \frac{V_f}{V_m}\int_a^r r^* s(r^*)dr^*\right] \quad . \tag{22d}$$

Note that continuity of normal tractions at $z = L/2 - l_s$, $0 \le r \le b$ requires that

$$f\left(\frac{L}{2}-l_s\right)=\frac{2\tau_s l_s V_f}{aSV_m E_m^*}\ , \tag{23a}$$

while continuity of shear tractions demands

$$\frac{\partial f(z=L/2-l_s)}{\partial z}=-\frac{2\tau_s V_f}{aSV_m E_m^*}\ . \tag{23b}$$

Equations (23a) and (23b) do *not* contradict each other, because any one of them can be employed to determine the unknown value of l_s. The remaining equation serves as a consistency condition.

Employing Eq. (22a) with the stress-strain relations (1), we obtain

$$\varepsilon_z^f=\frac{2\tau_s V_f}{aSV_m E_m^*}\left(\frac{L}{2}-z\right)\left[p(r)-\frac{q(r)}{Q}\left(P+S\frac{V_m E_m^*}{V_f E_f^*}\right)\right]+p(r)C$$

$$+\frac{(\sigma_a-\sigma_0)q(r)}{QV_f E_f^*}+\frac{t(r)(z-L/2+l_s)^2}{E_f^*}\ ,$$

which upon integration with respect to z yields

$$w_f=\frac{\tau_s V_f\left[(L-z)z-(L/2+l_s)(L/2-l_s)\right]}{aSV_m E_m^*}\left[p(r)-\frac{q(r)}{Q}\left(P+S\frac{V_m E_m^*}{V_f E_f^*}\right)\right]$$

$$+F\left(\frac{L}{2}-l_s\right)\left[p(r)-\frac{q(r)}{Q}\left(P+S\frac{V_m E_m^*}{V_f E_f^*}\right)\right]+p(r)Cz \tag{24}$$

$$+\frac{(\sigma_a-\sigma_0)q(r)z}{QV_f E_f^*}+\frac{t(r)(z-L/2+l_s)^3}{3E_f^*}\ .$$

The boundary condition (9a), namely $w_f(r,L/2)$ = constant $(0\le r<a)$, can be satisfied by an appropriate selection of $t(r)$. This is accomplished by utilizing Eq. (24) to evaluate the average value of w_f at $z=L/2$, then requiring that

$$w^f\left(r,\frac{L}{2}\right)=\overline{w}^f\left(z=\frac{L}{2}\right)\qquad(0\le r<a)\ . \tag{25}$$

The condition (25) yields

$$t(r)=\left\{-\left[\frac{\tau_s l_s^2 V_f}{aSV_m E_m^*}+F\left(\frac{L}{2}-l_s\right)\right]\left[p(r)-\frac{q(r)}{Q}\left(P+S\frac{V_m E_m^*}{V_f E_f^*}\right)+S\frac{V_m E_m^*}{V_f E_f^*}\right]\right.$$

$$\left.+\frac{L}{2}C[P-p(r)]+\frac{\sigma_a-\sigma_0}{2V_f E_f^*}\left[1-\frac{q(r)}{Q}\right]L\right\}\frac{3E_f^*}{l_s^3}\ . \tag{26}$$

Inspection of Eq. (26) shows that $\int_0^a rt(r)dr = 0$, which satisfies the requirements stated in Eqs. (21b) and (21e).

Turning to the matrix region ($L/2 - l_s \le z \le L/2$, $a < r \le b$), Eq. (22b) yields

$$\varepsilon_z^m = s(r)\frac{2\tau_s V_f}{aSV_m E_m^*}\left(\frac{L}{2} - z\right) + C \quad .$$

Whereby, upon integration with respect to z and imposition of continuity of w_m with $w_m(r, z = L/2 - l_s)$ given in Eq. (17c), we obtain

$$w_m = \frac{\tau_s V_f\left[(L-z)z - (L/2 + l_s)(L/2 - l_s)\right]}{aSV_m E_m^*} s(r) + s(r)F\left(\frac{L}{2} - l_s\right) + Cz \quad . \tag{27}$$

Note that, within the slip zone, $w_m(a,z) \neq w_f(a,z)$.

The radial displacements u_f and u_m within the slip zone are assumed to coincide with those given in Eq. (11). Consequently, we have within *both* contact and slip regions, namely for $0 \le z \le L/2$,

$$\begin{aligned} &\varepsilon_\theta^f = \varepsilon_r^f = A \quad , \qquad (0 \le r < a) \quad , \\ &\left.\begin{aligned} \varepsilon_r^m &= A + B\left(1 + \frac{a^2}{r^2}\right) \\ \varepsilon_\theta^m &= A + B\left(1 - \frac{a^2}{r^2}\right) \end{aligned}\right\} \quad (a < r \le b) \quad . \end{aligned} \tag{28}$$

The thermomechanical stresses that correspond to Eqs. (11) and (28), together with $\varepsilon_z^m = \varepsilon_z^f = \varepsilon_0$, are evaluated in Appendix A. The constants A and B are also determined in Appendix A, thus establishing the value of C that enters expressions (16), (17), (22), (24), and (27). It can be shown that incorporating the in-plane stresses into this analysis affects the results by an order of ν^2.

Also note that the in-plane stresses $\sigma_r^{f,m}$ and $\sigma_\theta^{f,m}$ that correspond to the displacements w_f and w_m prescribed in Eqs. (16c), (17c), (24), and (27) are no longer statically admissible, because those displacements depart from $w_f = w_m = \varepsilon_0 z$.

In the forthcoming analysis, we shall employ the minimum potential energy principle to determine $f(z)$ and utilize a numerical solution for analogous mechanical fields in Cartesian geometry to guide our choice of the shape functions $p(r)$, $q(r)$, and $s(r)$.

3.3 DETERMINATION OF THE FUNCTION $f(z)$

The field equation that governs the function $f(z)$ will be generated through minimizing the potential energy functional $\Pi(\underline{u})$ (Washizu 1975), where the displacements $\underline{u}$: u_m, u_f, w_m, and w_f are given by the kinematically admissible fields listed in Eqs. (11), (16c), (17c), (24), and (27). Employing expressions (1) and (2), we generate the strains $\varepsilon_r^{f,m} = \partial u^{f,m}/\partial r$, $\varepsilon_\theta^{f,m} = u^{f,m}/r$, $\varepsilon_z^{f,m} = \partial w^{f,m}/\partial z$, and $\gamma_{rz}^{f,m} = \partial w^{f,m}/\partial r$, which correspond to the above

displacements, and stresses that accord with those strains. Noting that $F(z) = \int_0^z f(s)ds$ and separating the volume of integration in to the fiber and matrix regions, we write

$$\Pi(F,f,l_s) = \int_0^a \int_0^{L/2} \mathcal{E}_f r\,dr\,dz + \int_a^b \int_0^{L/2} \mathcal{E}_m r\,dr\,dz$$

$$- \int_0^a \sigma_z^f\left(z=\frac{L}{2}\right) w_f\left(z=\frac{L}{2}\right) r\,dr + \int_{L/2-l_s}^{L/2} \left[w_f(r=a) - w_m(r=a)\right] a\tau_s\,dz \quad . \tag{29}$$

The above functional also can be divided among the regions of perfect contact and slip, whereby

$$\Pi = \int_0^{L/2-l_s} \pi_1[f(z),z,l_s]dz + \int_{L/2-l_s}^{L/2} \pi_2\left[F\left(\frac{L}{2}-l_s\right), z, l_s\right] dz \quad , \tag{30}$$

where

$$\pi_1 = \int_0^a \left[\mathcal{E}_f - \sigma_z^f\left(z=\frac{L}{2}\right)\varepsilon_z^f\right] r\,dr + \int_a^b \mathcal{E}_m\, r\,dr \quad , \quad 0 \le z \le \frac{L}{2} - l_s \quad , \tag{31}$$

while

$$\pi_2 = \int_0^a \left[\mathcal{E}_f - \sigma_z^f\left(z=\frac{L}{2}\right)\varepsilon_z^f\right] r\,dr + \int_a^b \mathcal{E}_m\, r\,dr$$

$$+ \frac{t(r=a)(z-L/2+l_s)^4\tau_s}{4l_s^3 E_f^*} \quad , \quad \frac{L}{2} - l_s \le z \le \frac{L}{2} \quad . \tag{32}$$

In Eqs. (30), (31), and (32),

$$\mathcal{E}_f = 0.5E_f^*\left[\left(\varepsilon_z^f\right)^2 + \left(\varepsilon_r^f\right)^2 + \left(\varepsilon_\theta^f\right)^2\right] + 0.5\mu_f\left(\gamma_{rz}^f\right)^2 + \frac{E_f^*\nu_f}{1-\nu_f}\left(\varepsilon_z^f\varepsilon_r^f + \varepsilon_r^f\varepsilon_\theta^f + \varepsilon_z^f\varepsilon_\theta^f\right)$$

$$- \frac{E_f^*(1+\nu_f)}{1-\nu_f}\alpha_f\Delta T\left(\varepsilon_z^f + \varepsilon_r^f + \varepsilon_\theta^f\right)$$

and

$$\mathcal{E}_m = 0.5E_m^*\left[\left(\varepsilon_z^m\right)^2 + \left(\varepsilon_r^m\right)^2 + \left(\varepsilon_\theta^m\right)^2\right] + 0.5\mu_m\left(\gamma_{rz}^m\right)^2 + \frac{E_m^*\nu_m}{1-\nu_m}\left(\varepsilon_z^m\varepsilon_r^m + \varepsilon_r^m\varepsilon_\theta^m + \varepsilon_z^m\varepsilon_\theta^m\right)$$

$$- \frac{E_m^*(1+\nu_m)}{1-\nu_m}\alpha_m\Delta T\left(\varepsilon_z^m + \varepsilon_r^m + \varepsilon_\theta^m\right) \quad .$$

Note, however, that the continuity conditions (23a, b) impose constraints on Π. To comply with those constraints, construct the modified functional Π^* expressed by

$$\Pi^* = \Pi + \lambda_1\left[f\left(\frac{L}{2}-l_s\right) - \frac{2\tau_s l_s V_f}{aSV_m E_m^*}\right]$$

$$+ \lambda_2\left[\frac{\partial f(z=L/2-l_s)}{\partial z} + \frac{2\tau_s V_f}{aSV_m E_m^*}\right] \quad , \tag{33}$$

where λ_1, λ_2 are Lagrange multipliers.

Evaluate now the variation $\delta\Pi^*$ and set $\delta\Pi^* = 0$ for a stationary value of Π^* [$f(z)$, l_s, λ_1, λ_2]. Performing the differentiations and integrations included in Eqs. (31) and (32), substituting the results in Eq. (30), and considering the independent variations δF, δl_s, $\delta\lambda_1$, and $\delta\lambda_2$ of Π^*, we obtain

$$\delta\Pi^*(f,l_s,\lambda_1,\lambda_2) = \int_0^{L/2-l_s}\left\{\left[\frac{\partial\pi_1}{\partial F(z)} - \frac{\partial^2\pi_1}{\partial f(z)\partial z}\right]\delta F(z) + \frac{\partial\pi_1}{\partial l_s}\delta l_s\right\} dz$$

$$+ \frac{\partial\pi_1(z = L/2 - l_s)}{\partial F}\delta F\left(\frac{L}{2} - l_s\right) - \frac{\partial\pi_1(z=0)}{\partial F}\delta F(0)$$

$$-\left[\pi_1\left(z = \frac{L}{2} - l_s\right) - \pi_2\left(z = \frac{L}{2} - l_s\right)\right]\delta l_s$$

$$+ \int_{L/2-l_s}^{L/2}\left[\frac{\partial\pi_2}{\partial F(L/2 - l_s)}\delta F\left(\frac{L}{2} - l_s\right) + \frac{\partial\pi_2}{\partial l_s}\delta l_s\right] dz$$

$$-\lambda_1\left[\frac{\partial f(z = L/2 - l_s)}{\partial z} + \frac{2\tau_s V_f}{aSV_m E_m^*}\right]\delta l_s$$

$$+\left[f\left(\frac{L}{2} - l_s\right) - \frac{2\tau_s l_s V_f}{aSV_m E_m^*}\right]\delta\lambda_1 - \lambda_2\left[\frac{\partial f^2(z = L/2 - l_s)}{\partial z^2}\right]\delta l_s$$

$$+\left[\frac{\partial f(z = L/2 - l_s)}{\partial z} + \frac{2\tau_s V_f}{aSV_m E_m^*}\right]\delta\lambda_2 \quad . \quad (34)$$

Collecting terms that correspond to the independent variations δf, ..., $\delta\lambda_2$, the governing equation for $f(z)$ reads

$$\frac{\partial f^2(z)}{\partial z^2} - (\beta_f/a)^2 f(z) + f_0(\beta_f/a)^2 = 0 \quad ,$$

$$0 \le z \le \frac{L}{2} - l_s \quad , \quad (35)$$

with the boundary conditions (23a) and (23b) restated as

$$f\left(\frac{L}{2} - l_s\right) = \frac{2\tau_s l_s V_f}{aSV_m E_m^*} \quad , \quad (36a)$$

$$\frac{\partial f(z = L/2 - l_s)}{\partial z} = -\frac{2\tau_s V_f}{aSV_m E_m^*} \quad . \quad (36b)$$

Assuming w_f and w_m odd in z [whereby $f(z)$ is even in z], the solution of Eq. (35) with Eq. (36a) reads

$$f(z) = f_0 - \left(f_0 - \frac{2\tau_s l_s V_f}{a S V_m E_m^*} \right) \frac{\cosh\left(\beta_f z/a\right)}{\cosh\left[\beta_f (0.5L - l_s)/a\right]} \quad . \tag{37}$$

The condition (36b) provides the expression that determines the length l_s of the slip zone

$$\beta_f \left(\frac{f_0}{a} - \frac{2\tau_s l_s V_f}{a^2 S V_m E_m^*} \right) \frac{\sinh\left[\beta_f (0.5L - l_s)/a\right]}{\cosh\left[\beta_f (0.5L - l_s)/a\right]} = \frac{2\tau_s V_f}{a S V_m E_m^*} \quad . \tag{38}$$

In performing the manipulations that lead to Eqs. (34), (35), and (37), we obtained

$$\beta_f = \left(\frac{C_1 + C_2}{C_3 + C_4} \right)^{0.5} \quad ,$$

where

$$C_1 = \mu_f \int_0^a \left[p'(r) - \frac{q'(r)}{Q} \left(P + S \frac{V_m E_m^*}{V_f E_f^*} \right) \right]^2 r \, dr \quad ,$$

$$C_2 = \mu_m \int_a^b \left[s'(r) \right]^2 r \, dr \quad ,$$

$$C_3 = \frac{E_f^*}{a^2} \int_0^a \left[p(r) - \frac{q(r)}{Q} \left(P + S \frac{V_m E_m^*}{V_f E_f^*} \right) \right]^2 r \, dr \quad ,$$

$$C_4 = \frac{E_m^*}{a^2} \int_a^b \left[s(r) \right]^2 r \, dr \quad ,$$

$$f_0 = \frac{-\mu_f}{(C_1 + C_2)} \int_0^a \left[p'(r) - \frac{q'(r)}{Q} \left(P + S \frac{V_m E_m^*}{V_f E_f^*} \right) \right] \left[p(r) C + \frac{(\sigma_a - \sigma_0) q(r)}{Q V_f E_f^*} \right] r \, dr \quad .$$

At this stage, it may be noted that adding a function $G(r, z)$, say, to σ_z^m in Eq. (20b), analogous to $H(r,z)$ in Eq. (20a), would lead to the requirements that $G(r, z = L/2 - l_s) = [\partial G(r, z = L/2 - l_s)]/\partial z = 0$, $\int_a^b r^* G(r^*, z) dr = 0$, as well as $G(r, z = L) = 0$. Upon incorporating $G(r, z)$ in the variational functional Π^*, the resulting Euler's equation on G, together with the above boundary conditions, would yield $G(r, z) \equiv 0$. Consequently, the choice of σ_z^m in Eq. (20b) is consistent with the remainder of the present formulation.

3.4 SELECTION OF THE SHAPE FUNCTIONS $p(r)$, $q(r)$, AND $s(r)$

The selection of the shape functions $p(r)$, $q(r)$ and $s(r)$ is guided by numerical results, obtained by means of the boundary element method, to a circumstance similar to the boundary value problem stated in Eqs. (1) through (10), except that the RVE is defined in Cartesian coordinates, namely $-L/2 < z < L/2$ with "fiber" and matrix regions extending over $|x| < a$ and $a < |x| \leq b$, respectively. The scheme and results are presented in Appendix B. In addition, the

choice of the above functions is influenced by analytical results obtained recently (Wijeyewickrema et al. 1990) to the problem of a single fiber contained within a concentrically cylindrical region of a multicracked matrix, but in the absence of interfacial slip. Accordingly, we choose

$$p(r)=\left(\frac{r}{a}\right)^n \quad , \tag{39a}$$

$$q(r)=1-\left(\frac{r}{a}\right)^n \quad , \tag{39b}$$

and

$$s(r)=1-D_1\left(1-\frac{a}{r}\right) \quad . \tag{39c}$$

The unknowns at this stage are l_s, D_1, and n, as well as A and B in Eqs. (A.1) and (A.2) (see Appendix A). These five unknowns can be determined by iteration employing Eqs. (A.18a, b), (A.9), (23a), or (23b) and the requirement that $\partial\sigma_z/\partial_z = 0$ at $z = L/2$, $r = 0$. The latter condition derives from the observation that $z = L/2$ is a symmetry plane in the present boundary value problem and should hold in addition to $\tau_{rz}(0, L/2) = 0$. In an exact solution, we would have $\partial\sigma_z/\partial z = 0$, $\tau_{rz} = 0$ at $z = L/2$ and $0 \le r < a$. However, the approximate character of our solution restricts our ability to satisfy the stated symmetry condition over the full range of r.

We have

$$\frac{\partial\sigma_z^f}{\partial z}\left(0,\ \frac{L}{2}\right)=D_2+D_3=0 \quad , \tag{40}$$

where

$$D_2=\frac{2\tau_s V_f E_f^*}{anSV_m E_m^*}\left(1+S\frac{V_m E_m^*}{V_f E_f^*}\right) \quad ,$$

$$D_3=\frac{6E_f}{nl_s^2}\left\{\left(1+S\frac{V_m E_m^*}{V_f E_f^*}\right)\left[\frac{\tau_s l_s^2 V_f}{aSV_m E_m^*}+F\left(\frac{L}{2}-l_s\right)\right]+\frac{L}{2}\left(\frac{\sigma_a-\sigma_0}{V_f E_f^*}-C\right)\right\} \quad .$$

To achieve computational efficiency, the iteration scheme assumes sequential values for the group of the unknowns (A, B, D_1) and subsequently for the pair (n, l_S). For example, for a given σ_a, we start with the uncracked state, whereby $D_1 = 0$ and A and B are determined from Eqs. (A.18a) and (A.18b). These values are then used for a given crack spacing L to solve simultaneously for n and l_S in Eqs. (23b) and (40). At this stage, we compute $\varepsilon_0 = \bar{\varepsilon}_z = \frac{2}{b^2 L}\int_0^b\int_{-L/2}^{L/2} \varepsilon_z(r,z)\, r\, dr\, dz$ and analogous values for $\bar{\sigma}_z^f$ and $\bar{\sigma}_z^m$, redefining new E_f and E_m in Eqs. (A.18a) and (A.18b) as $E_f = \bar{\sigma}_z^f / \bar{\varepsilon}_z$ and $E_m = \bar{\sigma}_z^m / \bar{\varepsilon}_z$ and recomputing A and B. The value of D_1 is determined by requiring that $\bar{\sigma}_z^m$ computed with $s(r)$, according to

Eq. (39c), agrees with $\overline{\sigma}_z^m$ evaluated from Eq. (A.9). The iteration proceeds until attaining desired accuracy. For cracks spaced at distances $L/2$, it is possible to start with values of A, B, and D_1, which correspond to the spacing L.

4. ANALYSIS OF MULTIPLE MATRIX CRACKING

Consider a fiber-reinforced ceramic composite, subjected to an applied stress σ_a, with planar matrix cracks spaced at distances L apart. Let new planar cracks propagate quasistatically in a straight front in the x-direction midway between the existing cracks, namely at spacings of $L/2$ apart, as shown in Fig. 4.1.

Assume that the volume of the fiber-reinforced composite is filled completely by the RVEs, as shown in Fig. 2.1. In this case, the criterion for the formation of new matrix cracks can be derived by comparing energy levels in "upstream" and "downstream" RVEs. The upstream RVE has cracks spaced at distances $L/2$, which we denote by "State II," while the downstream element has cracks spaced L apart, designated by "State I."

Let $\mathcal{G}_m^c$ be the critical energy release rate associated with matrix cracking, and let U denote strain-energy density; then, in analogy with Budiansky, Hutchinson, and Evans (1986), the transition from State I to State II is governed, formally, by the criterion

$$\int_{-L/2}^{L/2}\int_0^b [U_{\mathrm{II}}(r,z)-U_{\mathrm{I}}(r,z)]r\,dr\,dz = \pi\left(b^2-a^2\right)\mathcal{G}_m^c \quad . \tag{41}$$

Let V and S denote the volume and outer surface of the RVE, and let t_i be the tractions on S. Employing the divergence theorem, we have

$$\int_V (U_{\mathrm{II}}-U_{\mathrm{I}})\,dV = \frac{1}{2}\int_V \left(\sigma_{ij}^{\mathrm{II}}\varepsilon_{ij}^{\mathrm{II}}-\sigma_{ij}^{\mathrm{I}}\varepsilon_{ij}^{\mathrm{I}}\right)dV = \frac{1}{2}\int_S \left(t_i^{\mathrm{II}}u_i^{\mathrm{II}}-t_i^{\mathrm{I}}u_i^{\mathrm{I}}\right)dS \quad .$$

Splitting the left side of Eq. (41) between the fiber and matrix regions, we have

$$\frac{1}{2}\int_{S_f}\left(t_{if}^{\mathrm{II}}u_{if}^{\mathrm{II}}-t_{if}^{\mathrm{I}}u_{if}^{\mathrm{I}}\right)dS_f+\frac{1}{2}\int_{S_m}\left(t_{im}^{\mathrm{II}}u_{im}^{\mathrm{II}}-t_{im}^{\mathrm{I}}u_{im}^{\mathrm{I}}\right)dS_m = \pi\left(b^2-a^2\right)\mathcal{G}_m^c \quad . \tag{42}$$

In State I, the surface S_f consists of the horizontal circular regions at $z = \pm L/2$ and the cylindrical boundary $r = a$, $|z| \le L/2$, which consists of slip zones $r = a$, $L/2 - l_s < |z| < L/2$, and a contact region $|z| \le L/2 - l_s$. In State II, the cylindrical boundary of S_f contains a new slip zone at $r = a$, $|z| < l_s$, whereby the contact region reduces to $l_s \le |z| \le L/2 - l_s$. Similarly, in State I, the surface S_m consists of traction-free crack surfaces at $z = \pm L/2$, $a < r < b$, a cylindrical boundary $r = a$, $|z| \le L/2$, of common features to S_f, and a traction-free boundary at $r = b$, $|z| \le L/2$. In State II, the boundary S_m contains a new traction-free crack at $z = 0$, $a < r < b$, as well as a new slip zone at $r = a$, $|z| < l_s$, commensurate with S_f.

Consequently, Eq. (42) reduces to the following expression:

$$\pi b^2\sigma_a\left[w_f^{\mathrm{II}}\left(z=\frac{L}{2}\right)-w_f^{\mathrm{I}}\left(z=\frac{L}{2}\right)\right]-U_{\mathrm{slip}} = \pi\left(b^2-a^2\right)\mathcal{G}_m^c \quad , \tag{43}$$

where

$$U_{\mathrm{slip}} = 2\pi a\tau_s\left\{\int_{L/2-l_s}^{L/2}\left[\Delta w^{\mathrm{II}}(a,z)-\Delta w^{\mathrm{I}}(a,z)\right]dz+\int_0^{l_s}\Delta w^{\mathrm{II}}(a,z)dz\right\} , \tag{44}$$

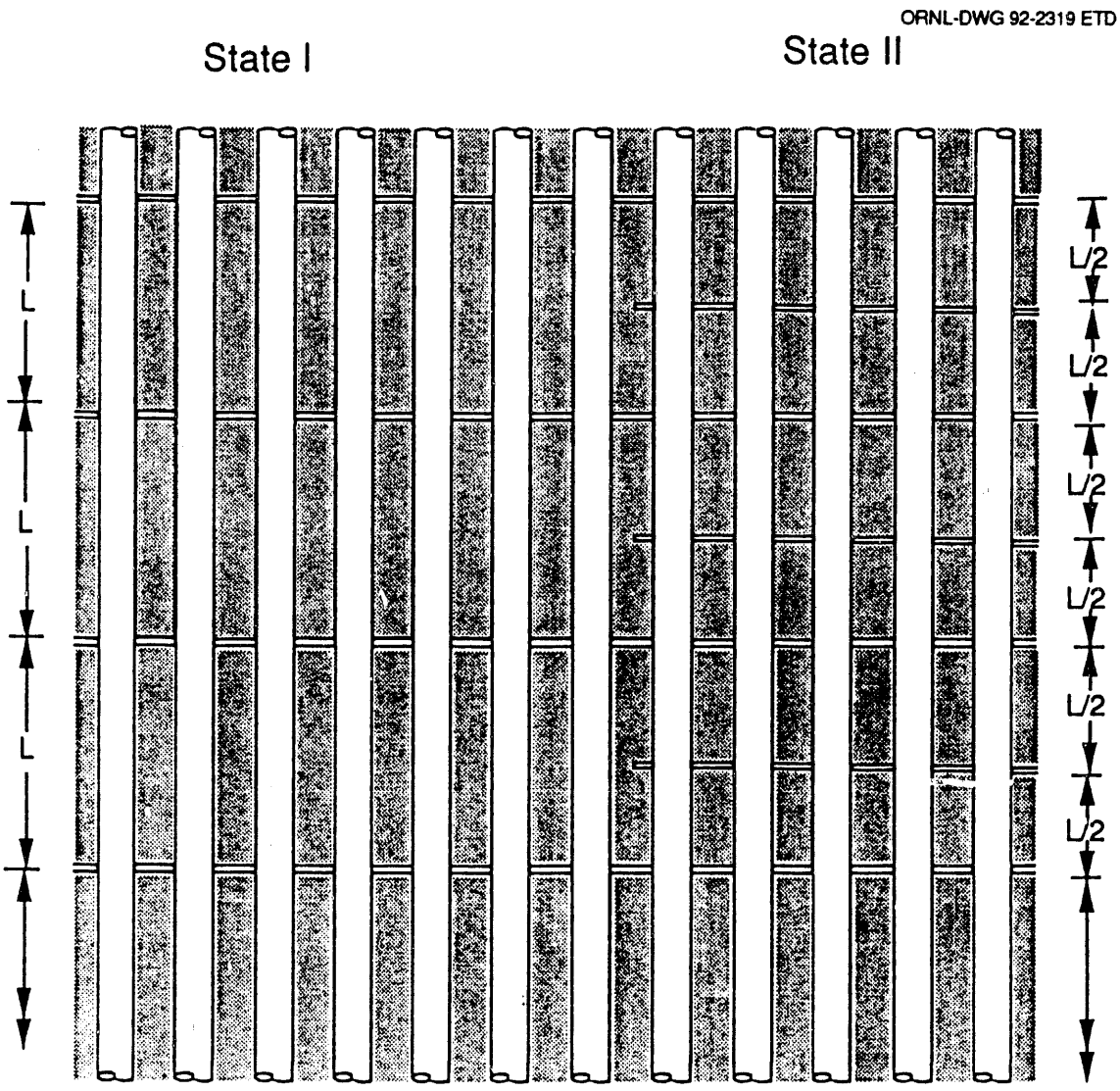

Fig. 4.1. Two states of matrix fractures in continuous fiber-reinforced ceramic composites. State I: Cracks spaced at distance *L*. State II: Cracks spaced at distance *L*/2.

where $\Delta w(a, z) = w_m(a, z) - w_f(a, z)$, as defined earlier in this work.

Equation (43) can be viewed as a criterion to determine the magnitude of σ_a^c associated with transition from State I to State II. Analogous transitions occur from "state $(N + 1)$" to "state $(N + 2)$," $N = 1, 2, \ldots$, when average crack spacing increases from $(L/2^N)$ to $(L/2^{N+1})$ with applied stress value $(\sigma_a^c)_N$. Between transitions, namely for $(\sigma_a^c)_N < \sigma_a < (\sigma_a^c)_{N+1}$, and under monotonically increasing σ_a, the composite sustains monotonic, continuously increasing strains.

The formal criterion (41) and the attendant results expressed in Eqs. (43) and (44) are subjected to the thermodynamic requirements of irreversibility of dissipation. In the present case, this requirement implies that U_{slip} must be a nondecreasing function of the applied stress σ_a. Specifically, under monotonically increasing σ_a as well as during transitions between fracture

states, the lengths l_s of the slip zones cannot decrease in size. Consequently, our computational solution to Eq. (43) included the requirement that the lengths l_s of the slip zones associated with State I (say) at $\sigma_a = \sigma_a^c - \varepsilon$ do not decrease upon the transition to State II (say) at $\sigma_a = \sigma_a^c - \varepsilon$.*

In the computations of the results exhibited below, we employed the following values for the thermomechanical properties of the fibers and the matrix (unless stated otherwise): E_f = 200 GPa, E_m = 85 GPa, ν_f = 0.1, ν_m = 0.1, V_f = 0.4, $a = 8.0 \times 10^{-6}$ m, $\mathcal{J}_m^c$ = 44 N/m, and T = –550°C. Also, when considering $\alpha_f > \alpha_m$, we took $\alpha_f = 6.0 \times 10^{-6}$/°C, and $\alpha_m = 3.0 \times 10^{-6}$/°C, while for $\alpha_m > \alpha_f$ we employed $\alpha_f = 3.0 \times 10^{-6}$/°C, and $\alpha_m = 6.0 \times 10^{-6}$/°C. These values correspond to SiC/LAS ceramic composites.

Various values were selected for the τ_s and $\mathcal{J}_m^c$ to demonstrate their influence on the stress-strain response of the composite material. Furthermore, we chose (somewhat arbitrarily) the spacing $L \equiv 30{,}000a$ as the initial distance between adjacent cracks to lead off the computations of the stress-strain curves. For the specific examples considered herein, the earliest noticeable departure from linearity occurred at $L \sim 128a$ and larger values of L yielded stress-strain curves indistinguishable from those shown below.† Results are exhibited in Figs. 4.2 through 4.9.

The predicted stress-strain curves, with longitudinal and transverse strains denoted by ε_L and ε_T, are shown in Figs. 4.2 through 4.5. The influence of τ_s is exhibited in Fig. 4.2 (where $\alpha_f = \alpha_m$), the effect of $\mathcal{J}_m^c$ is shown in Fig. 4.3 (with τ_s = 0.02 GPa and $\alpha_f = \alpha_m$), while the effects of thermal mismatch are demonstrated in Fig. 4.4 (with τ_s = 0.02 GPa). Here, and elsewhere in the present work, these effects are calculated for a temperature drop ΔT = –550°C below a stress-free initial condition at an elevated temperature. Figure 4.5 shows that, for a certain combination of material parameters, it is indeed possible to attain a sign reversal in the lateral strain, as observed in Fig. 1.2. In this figure, $\mathcal{J}_m^c$ = 5 N/m and τ_s = 0.2 GPa.

The radial variations of σ_z^f at the plane of the matrix crack, and its dependence on the residual thermal stress, are shown in Figs. 4.6a and 4.6b for two levels of applied load σ_a and with τ_s = 0.02 GPa. Note that all models based on shear-lag neglect this radial variation and, when matrix cracks are present, cannot account for residual thermal stress effects. The effect of τ_s on $\sigma_z^f(r/a, \tilde{z}/a)$ is demonstrated in Fig. 4.7 by plotting profiles of these stresses at various distances $\tilde{z}/a$ from the plane of the matrix crack (i.e., $\tilde{z} = z + L/2$) vs r/a. Thermal effects are discarded in this figure.

Larger values of τ_s are associated with larger amplifications and higher peak values of σ_z^f near the plane of the matrix crack, but these amplifications reduce more quickly to the undisturbed background levels upon moving away from the matrix crack. In addition, larger values of τ_s are accompanied by shorter slip zones l_s and larger spacings L between matrix cracks. Figures 4.8a, 4.8b, and 4.9 exhibit further details about factors that affect L and l_s.

Note that Figs. 2.1 and 4.1 represent a highly idealized circumstance of equal fiber spacings L and $L/2$. It is more reasonable to assume that in realistic circumstances the crack spacings at each stress level σ_a range between L_z and $2L_z$, with an average value of $L = 3/2L_z$. This suggests that the length L employed in this work should be interpreted to be 50% larger than the average crack spacing. More refined considerations (Kimber and Keer 1982) suggest that $L = 1.337L_z$.

---

*It turned out that at $\sigma_a = \sigma_a^c$, the slip zones near the new cracks in State II (say) had lengths $l_s' = l_s$.

†This observation explains why the occurrence of early matrix cracks cannot be detected from stress-strain response. In addition, it appears that deterministic analyses that aim at predicting conditions for the onset of first matrix cracking may be futile, because the early state of cracking is entirely governed by stochastic parameters such as the random geometry of initial flaws within the composite.

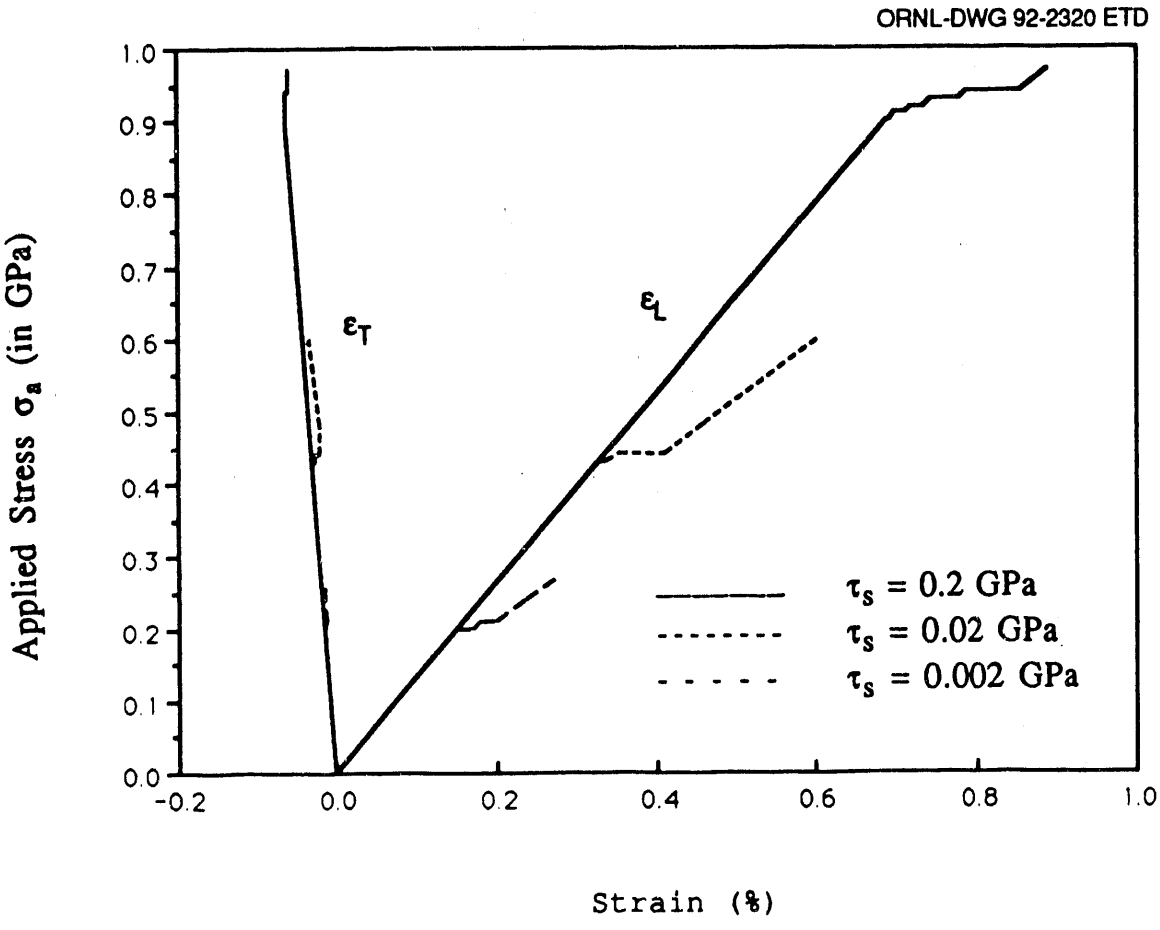

Fig. 4.2. The effect of interfacial shear strength, τ_s, on the stress-strain response of continuous fiber-reinforced ceramic composites (with $\alpha_f = \alpha_m$).

The value of $\mathcal{G}_m^c$ was selected, ad hoc, to be the same as obtained in the monolithic ceramic matrix. In principle, this value is stochastic rather than deterministic. In addition, it is not certain that the in situ value of $\mathcal{G}_m^c$ within a composite is in fact the same as for the monolithic material.

The stress-strain plots in Figs. 4.2, 4.3, 4.4, and 4.5 were terminated when $l_s = L/2$, namely when slip occurred over the entire fiber/matrix interface. It seems that beyond that range the stress-strain behavior is governed by fiber failures.

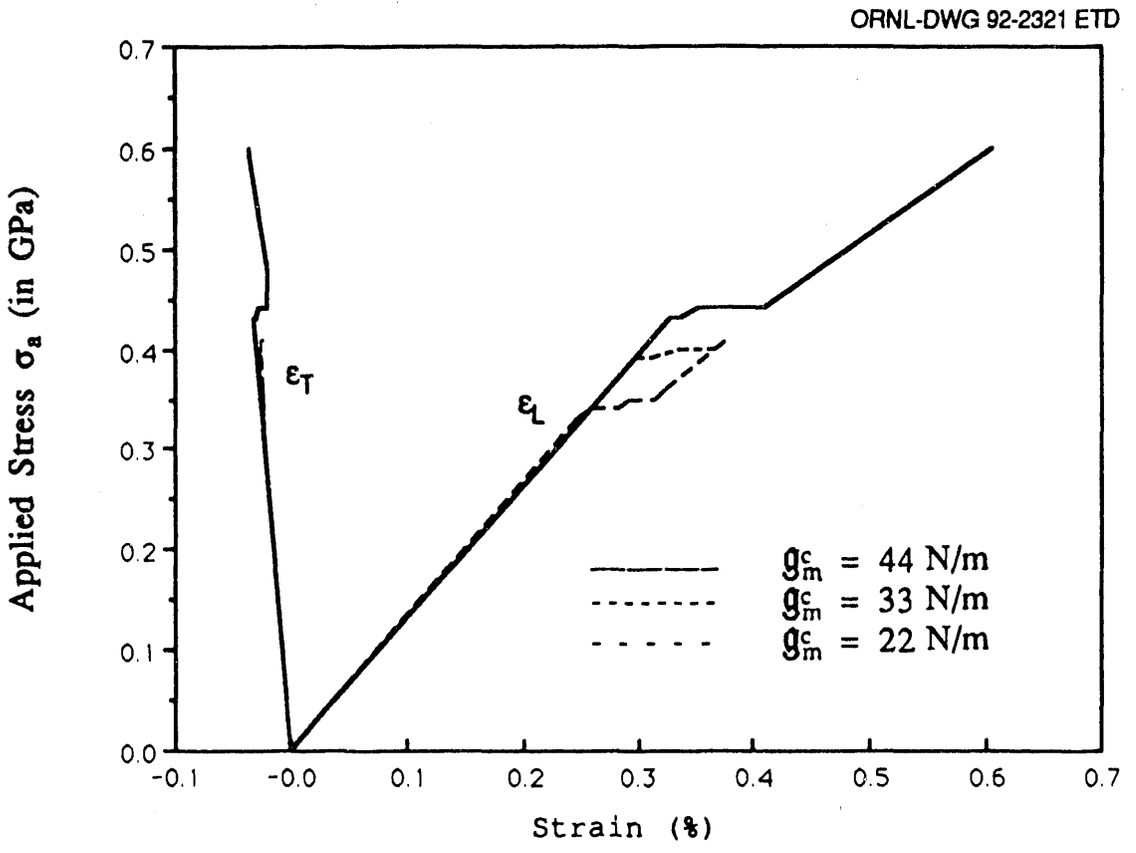

Fig. 4.3. Effects of matrix fracture toughness on stress-strain response of continuous fiber-reinforced ceramic composites ($\tau_s = 0.02$, $\alpha_f = \alpha_m$).

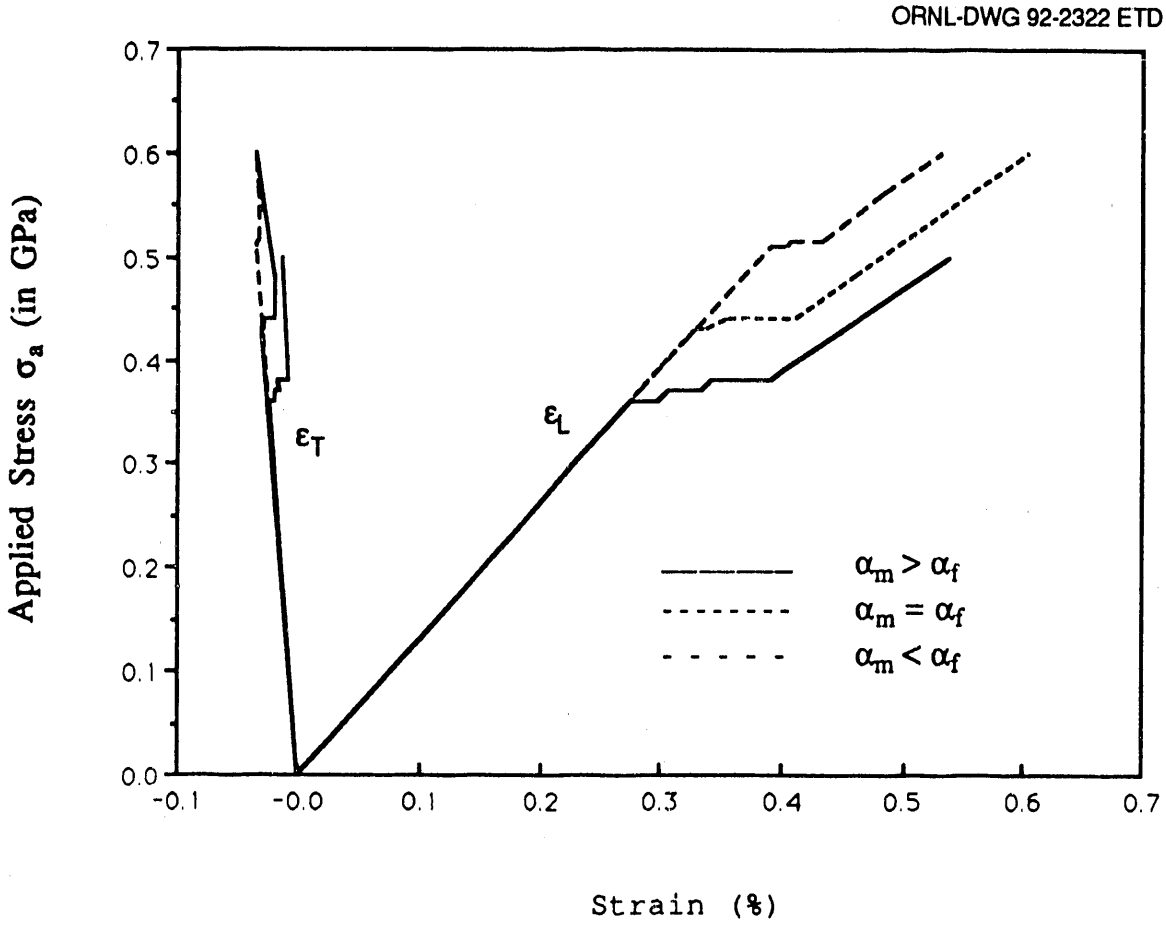

Fig. 4.4. Effect of thermal expansions on stress-strain response of continuous fiber-reinforced ceramic composites ($\tau_s = 0.02$).

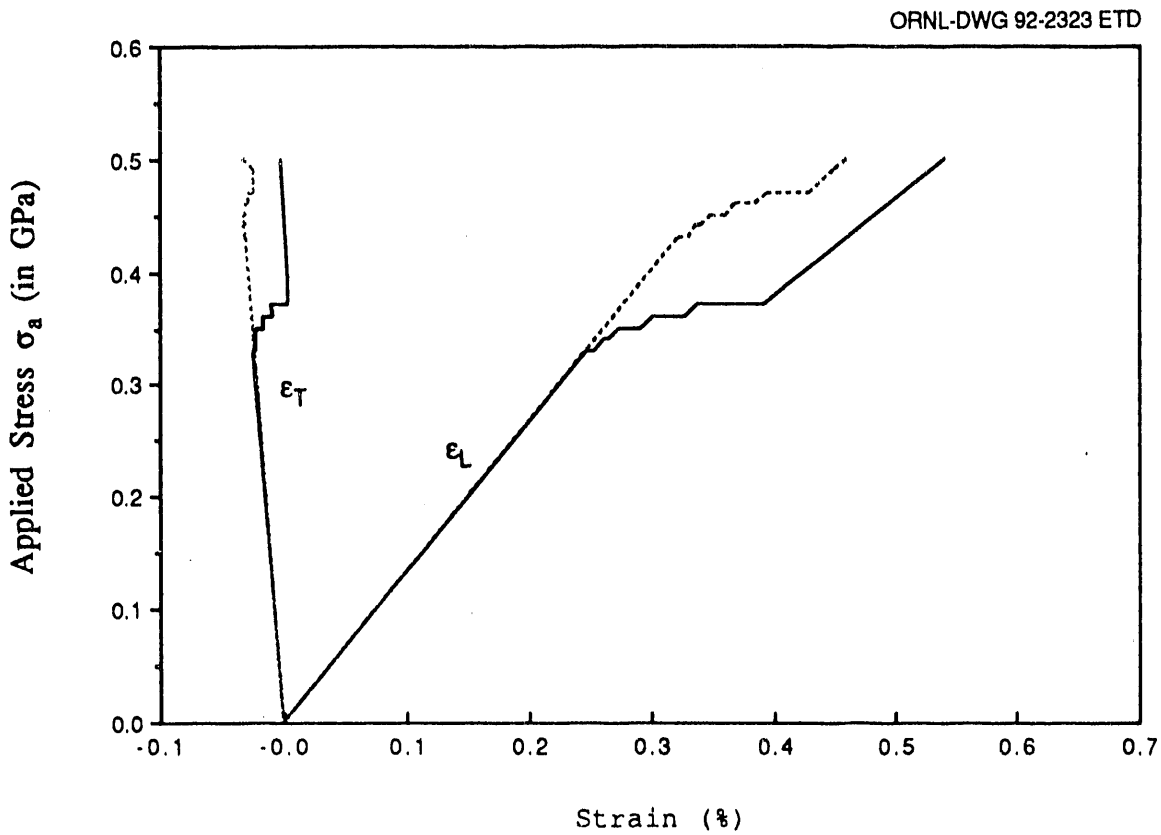

Fig. 4.5. Stress-strain response at $\mathcal{G}_m^c$ = 5 N/m and τ_s = 0.2 GPa for $\alpha_m > \alpha_f$ (——) and $\alpha_m = \alpha_f$ (- - - -).

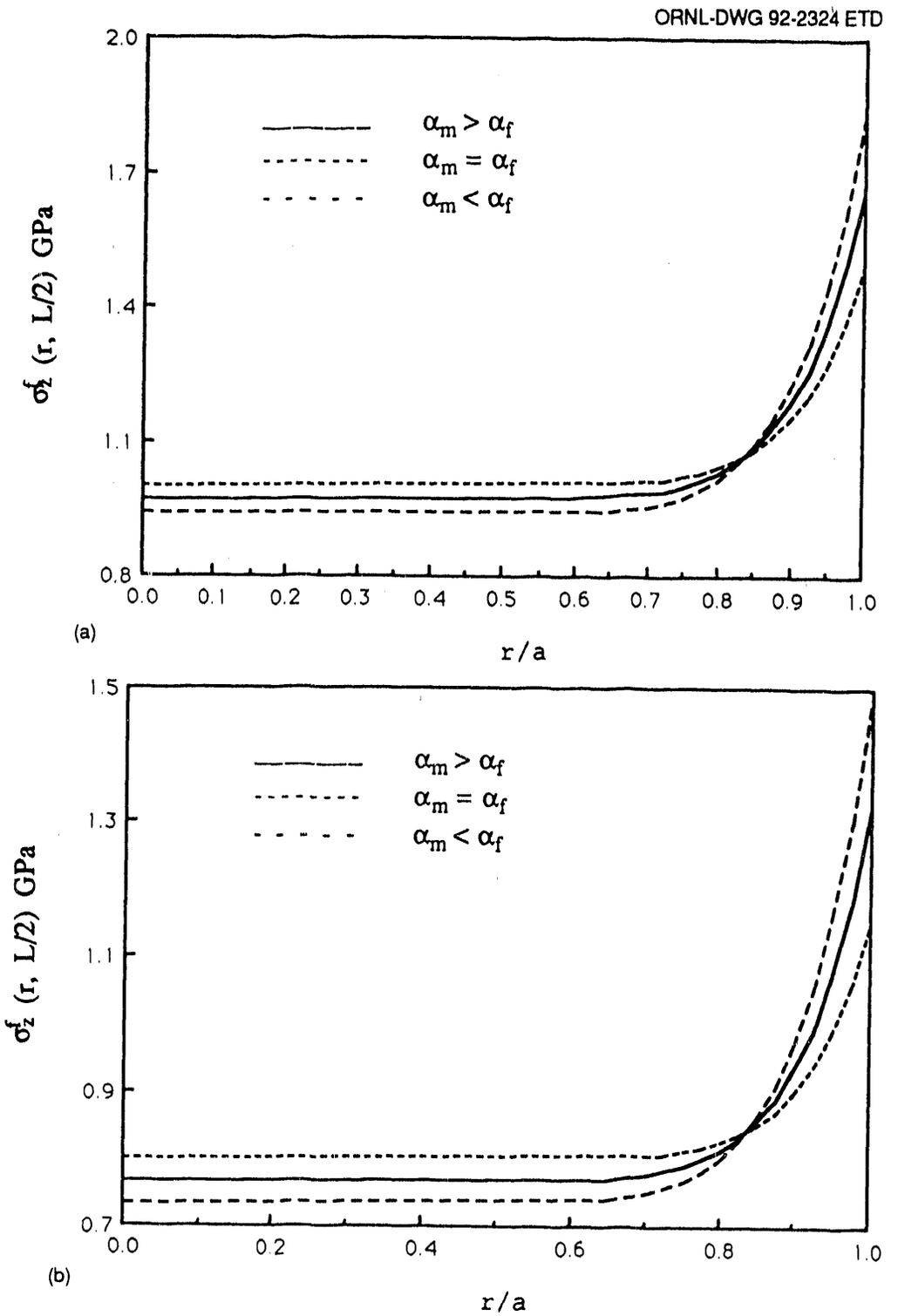

Fig. 4.6. Effect of thermal expansions on stress distribution within fiber (at plane of matrix cracks) (a) σ_a = 0.43 GPa (τ_s = 0.02 GPa), (b) σ_a = 0.34 GPa (τ_s = 0.02 GPa).

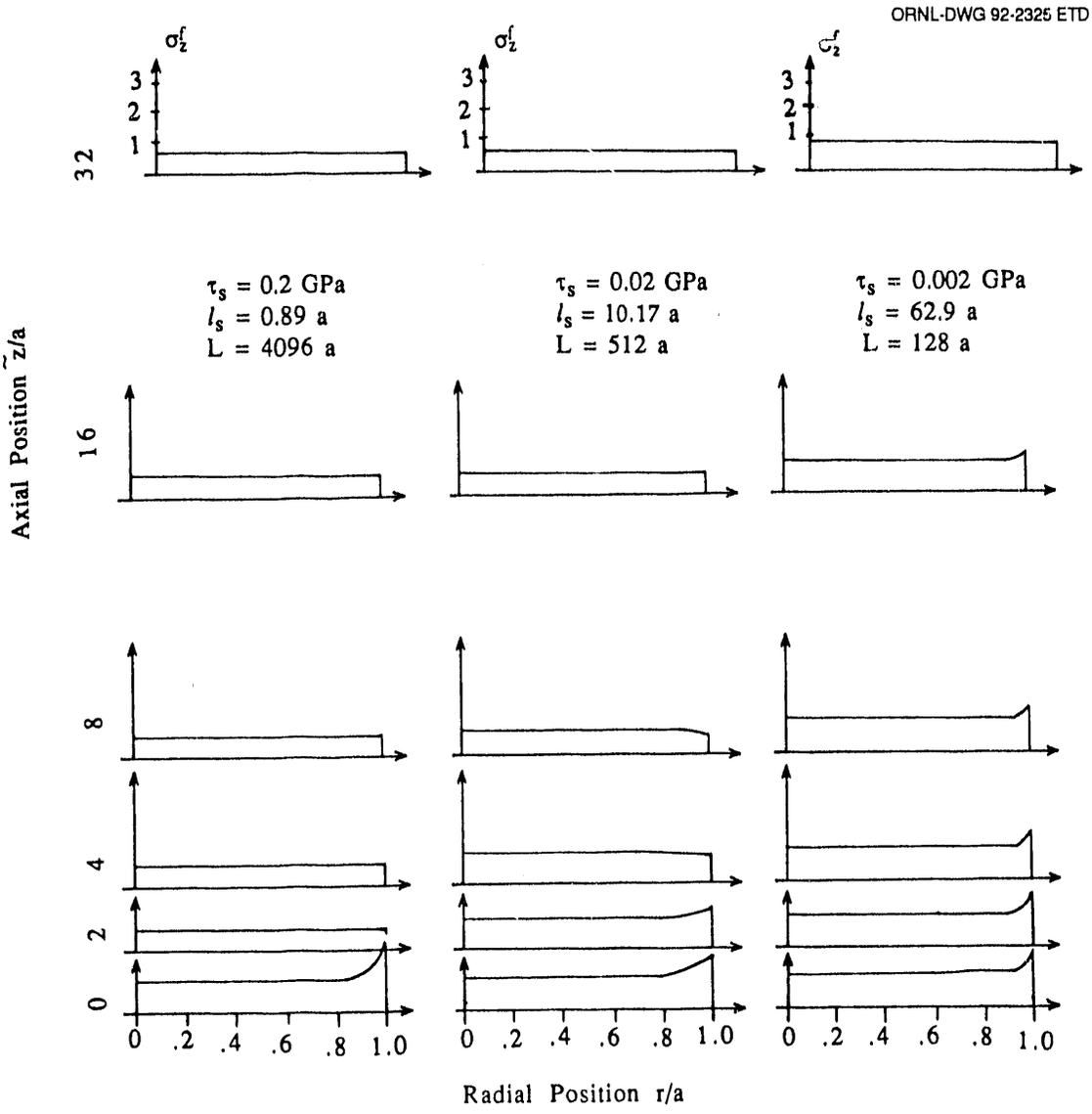

Fig. 4.7. Dependence of stress distributions within fibers on the interfacial shear strength τ_s. Shown are profiles of $\sigma_z^f(r/a, \tilde{z}/a)$ (in GPa) at various distances, $\tilde{z}/a$, from the matrix crack, for $\sigma_a = 0.43$ GPa.

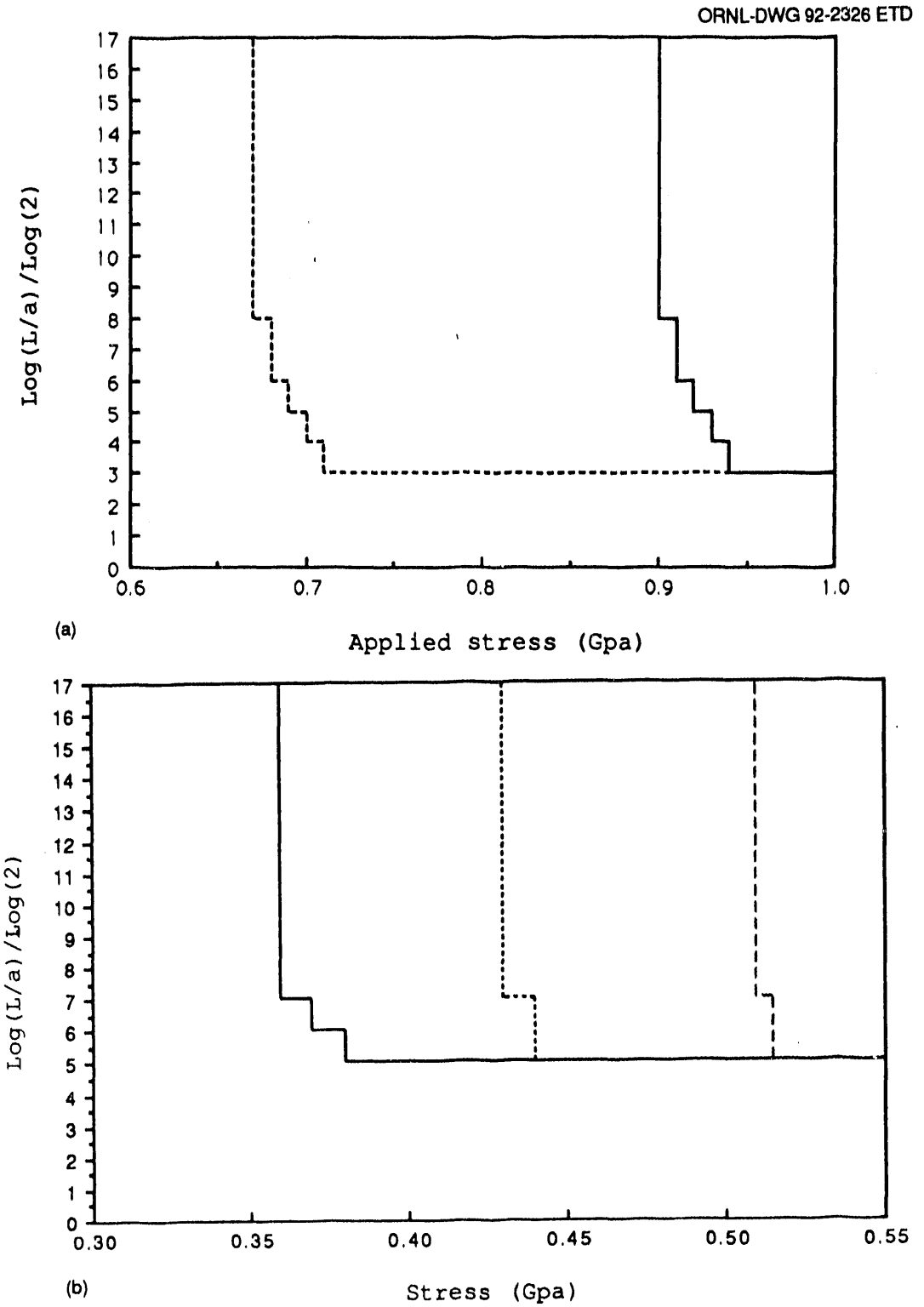

Fig. 4.8. Crack spacing, L, in terms of log (L/a)/log(2) vs applied stress for (a) τ_s = 0.2 GPa. Cases of $\alpha_m = \alpha_f$ (solid line) and $\alpha_m > \alpha_f$ (dashed line). (b) τ_s = 0.02 GPa. Cases of $\alpha_m > \alpha_f$ (————), $\alpha_m = \alpha_f$ (--------), and $\alpha_m < \alpha_f$ (- - - - - -).

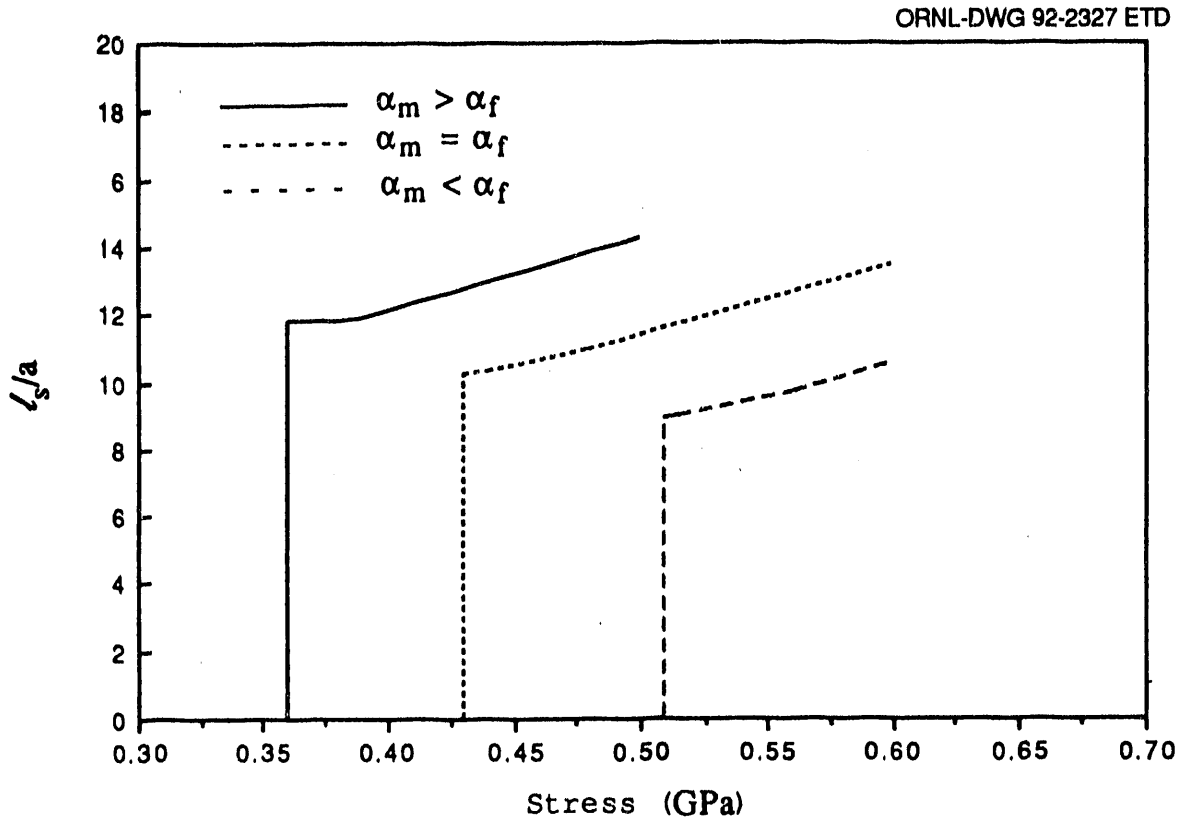

Fig. 4.9. Length of slip zone, l_s, vs applied stress for τ_s = 0.02 GPa. Cases of $\alpha_m > \alpha_f$ (——), $\alpha_m = \alpha_f$ (-----), and $\alpha_m < \alpha_f$ (- - - -).

5. STATISTICAL PREDICTIONS OF FIBER FAILURES

It is generally agreed that fiber failure is controlled by a statistical distribution of microstructural surface flaws (Thouless and Evans 1988, Sutcu 1989). The effect of these flaws on the statistics of fiber strength is commonly represented by a Weibull distribution, which is also adopted in the present case. Accordingly, the probability P_f of fiber failure is expressed by

$$P_f = 1 - \exp\left\{-2\pi aN \int_{-L/2}^{L/2} \left[\frac{\sigma_z^f(a,z)}{\sigma_0}\right]^M dz\right\} , \tag{45}$$

where $2\pi aL$ is the outer cylindrical surface of the fiber within an RVE of length L; $N = L^*/L$ is the number of matrix cracks in a test coupon of length L^*; M is the Weibull modulus that, for ceramic fibers, has values between 8 and 10; and σ_0 is a Weibull parameter that represents, approximately, the mean value of the failure stress.

Note also that, because $M > 1$, we have at any cross section $A_f = \pi a^2$ within the RVE $\int_{A_f} [\sigma_z^f(r;z) - \bar{\sigma}_z^f(z)]^M dA_f > 0$, where $\bar{\sigma}_z^f(z)$ is the average stress at any z. It follows that fiber failure predictions based on models that do not detail the radial variation of $\bar{\sigma}_z^f$ are likely to grossly underestimate the failure probability. This occurs for the commonly employed shear-lag model.

The probabilities P_f of fiber failure under increasing levels of applied stress σ_a were computed in accordance with Eq. (45), employing values for $\sigma_z^f(a, z)$ and L determined by the formulations in Sects. 3 and 4. We also employed the values $M = 10$ and $\sigma_0 = 0.4$ GPa $m^{2/M}$.

Some aspects of the dependence of P_f on the interfacial shear strength τ_s are exhibited in Fig. 5.1, where P_f is plotted vs σ_a for $\tau_s = 0.2$, 0.02, and 0.002 GPa. In these computations, it was also assumed that $\alpha_f = \alpha_m$. The effect of residual thermal stresses, with $\tau_s = 0.02$ GPa, is shown in Fig. 5.2, while the significant effect of the radial variation of σ_z^f on P_f is demonstrated in Figs. 5.3a and 5.3b. Note that computations based on radially averaged values $\bar{\sigma}_z^f(z)$ will underpredict the probabilities of fiber failure.

As noted by Schwietert and Steif (1990), multiple failures may occur within a single fiber. Such failures and, especially, denser crack spacing as $P_f \to 1$ would necessitate the consideration of fiber failure interactions. Fiber failures will modify the stress-strain curves shown in Figs. 4.2 through 4.5 and, most importantly, will introduce another energy-absorbing mechanism, commonly referred to as "fiber pull-out," that adds significantly to the toughening of the composite.

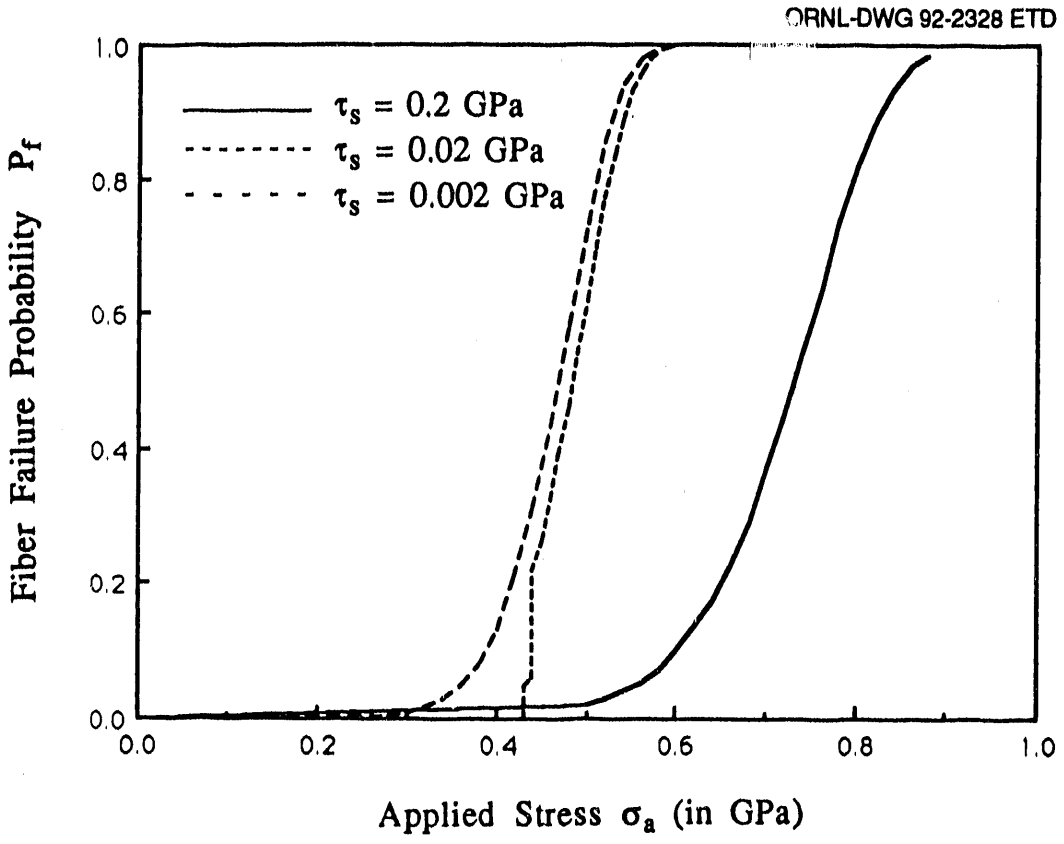

Fig. 5.1. The effect of interfacial shear stress, τ_s, (in GPa) on the probability of fiber failure, accounting for radial variation in fiber stress distribution (with $\alpha_f = \alpha_m$).

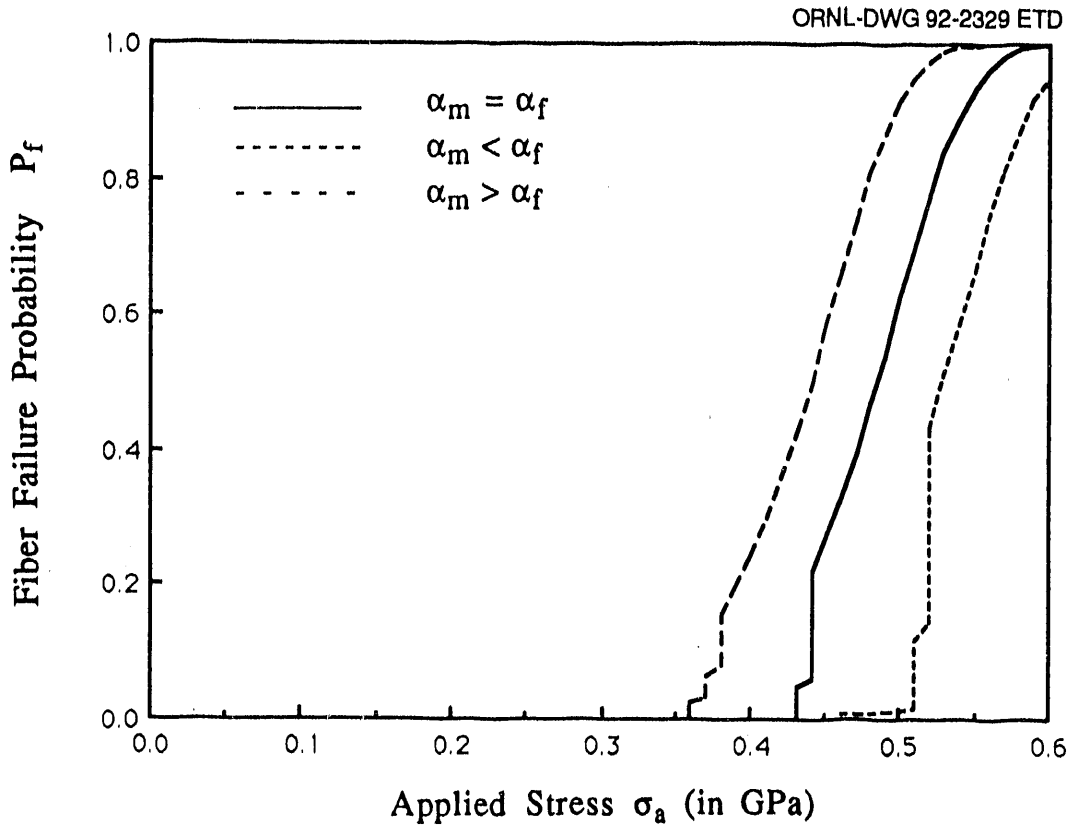

Fig. 5.2. Probability of fiber failure vs applied stress and its dependence on thermal expansions (τ_s = 0.02 GPa).

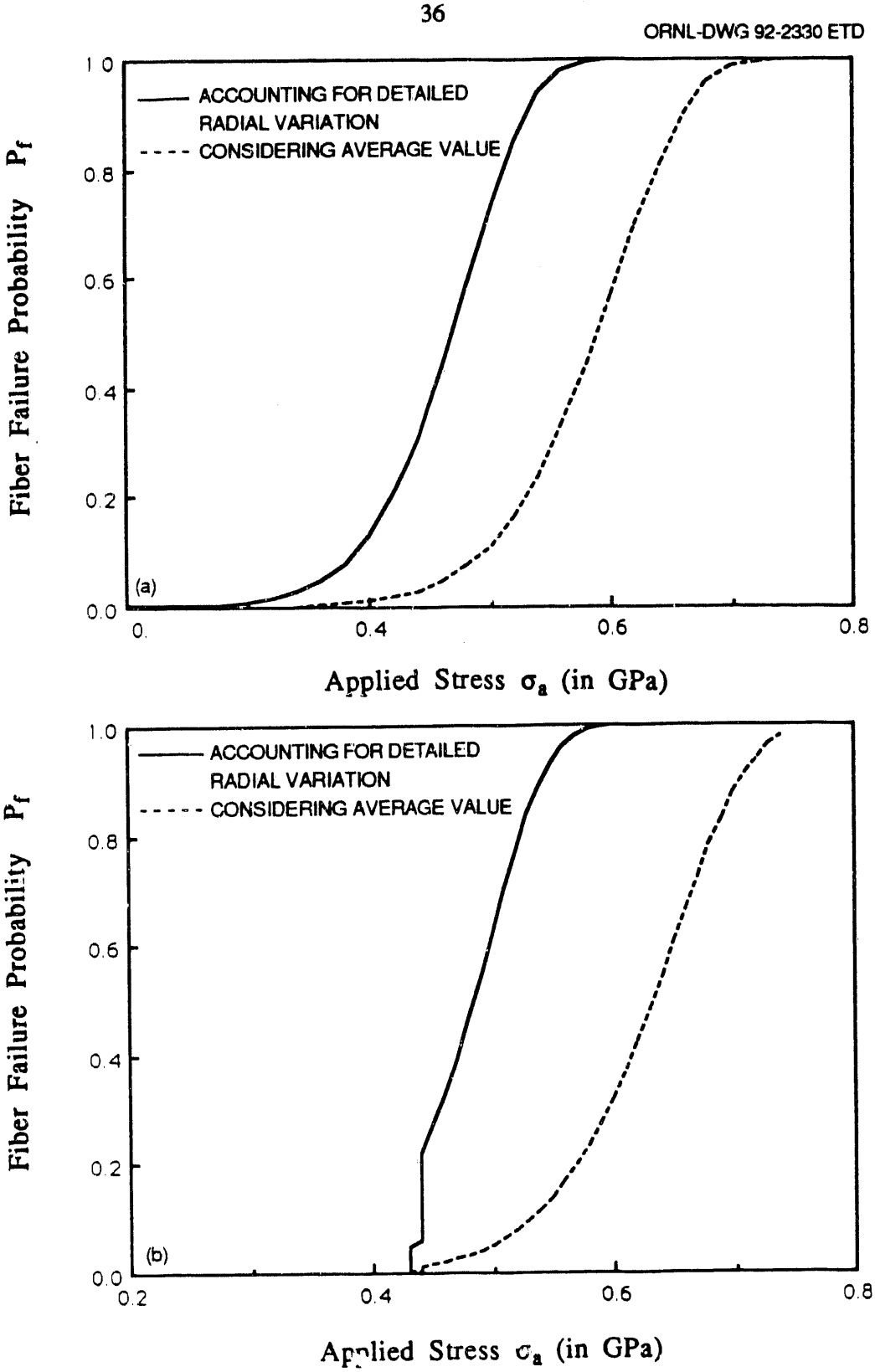

Fig. 5.3. The effect of radial variation of fiber stresses on the probability of fiber failure (a) (τ_s = 0.002 GPa, $\alpha_m = \alpha_f$), (b) (τ_s = 0.02 GPa, $\alpha_m = \alpha_f$).

6. SOME CONSIDERATIONS OF FIBER PULL-OUT ENERGY

It is now hypothesized that a negligible amount of energy is dissipated when a fiber break occurs within the perfectly bonded contact region of an RVE, namely, at location z equal or equivalent to $0 < z < L/2 - l_s$. In these circumstances, the load borne by the fiber is transferred to the matrix, and the effect of the fiber break is localized within just a few fiber diameters (Kelly and MacMillan 1986). In addition, because the site of such a fiber crack is somewhat far from the location of any matrix crack, interactive failure is less likely to occur.

On the other hand, when fiber failure occurs within the slip zone, that is, at a location z_{fb}, where $L/2 - l_s < z_{fb} < L/2$, the effect of the fiber break extends all the way to $z = L/2$. The reason for this longer range effect is demonstrated in Fig. 6.1.

Accordingly, at $z_{fb} < z < L/2$, $r = a$, the shear stresses τ_{fb} due to a fiber break at $z = z_{fb}$ would point in the same direction as the shear stresses τ_s caused by the pre-existing matrix crack at $z = L/2$, while for $z > L/2$ and $z < z_{fb}$, τ_{fb} and τ_s point in opposite directions. However, because the interfacial shear stresses cannot exceed τ_s, the fiber region $z_{fb} < z < L/2$, $0 \le r < a$, will contract without frictional resistance at $r = a$, namely as a "free-standing column."

Because fiber failure in the slip zones is a random event, we now evaluate the probability P_{fs} of such occurrence. This quantity is to be contrasted with P_f, the probability of fiber failure anywhere along its length, given in Eq. (45).

For that purpose, we introduce the function

$$P_f(0,z) = 1 - \exp\left\{-2\pi a \int_0^z \left[\frac{\sigma_z^f(a,\hat{z})}{\sigma_0}\right]^M d\hat{z}\right\} \quad , \tag{46}$$

which expresses the probability of fiber failure within the interval $(0,z)$.

Accordingly, the probability of failure within the interval $z_1 < z < z_2$ is given by

$$P_f(z_1,z_2) = \int_{z_1}^{z_2} \frac{\partial P_f(0,z)}{\partial z}\, dz$$

$$= \exp\left\{-2\pi a \int_0^{z_1} \left[\frac{\sigma_z^f(a,z)}{\sigma_0}\right]^M dz\right\} - \exp\left\{-2\pi a \int_0^{z_2} \left[\frac{\sigma_z^f(a,z)}{\sigma_0}\right]^M dz\right\} \tag{47}$$

$$= \exp\left\{-2\pi a \int_0^{z_1} \left[\frac{\sigma_z^f(a,z)}{\sigma_0}\right]^M dz\right\}\left(1 - \exp\left\{-2\pi a \int_{z_1}^{z_2} \left[\frac{\sigma_z^f(a,z)}{\sigma_0}\right]^M dz\right\}\right) .$$

It can be readily verified that $P_f(z_1, z_2)$ possesses the required property that, for any $z_1 < z_2 < z_3$,

$$P_f(z_1,z_3) = P_f(z_1,z_2) + P_f(z_2,z_3) \quad , \tag{48}$$

which is consistent with the Weibull statistical approach employed in the present framework

ORNL-DWG 92-2331 ETD

State "0": No Cracks

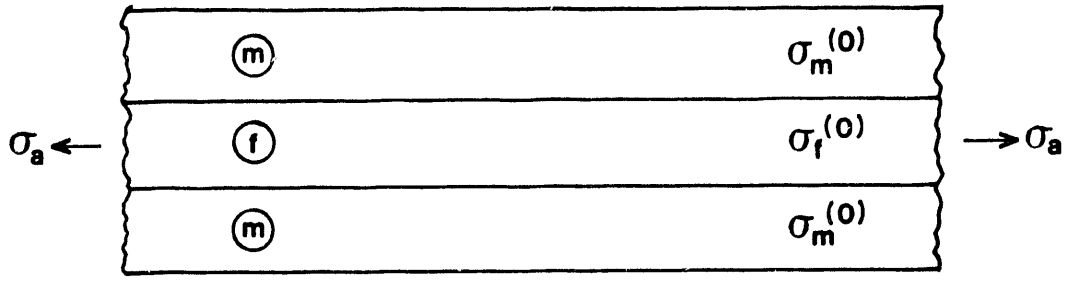

State "1": A Matrix Crack at z = L/2 with Interfacial Slip Zones

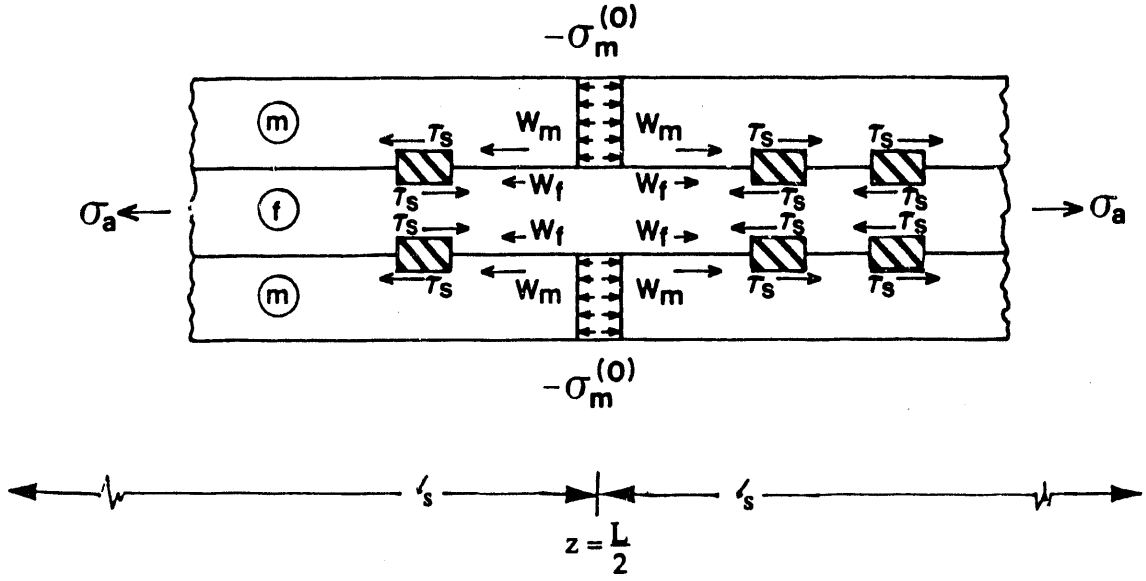

State "2": Fiber Break at z = z_{fb} Superimposed on Matrix Crack at z = L/2

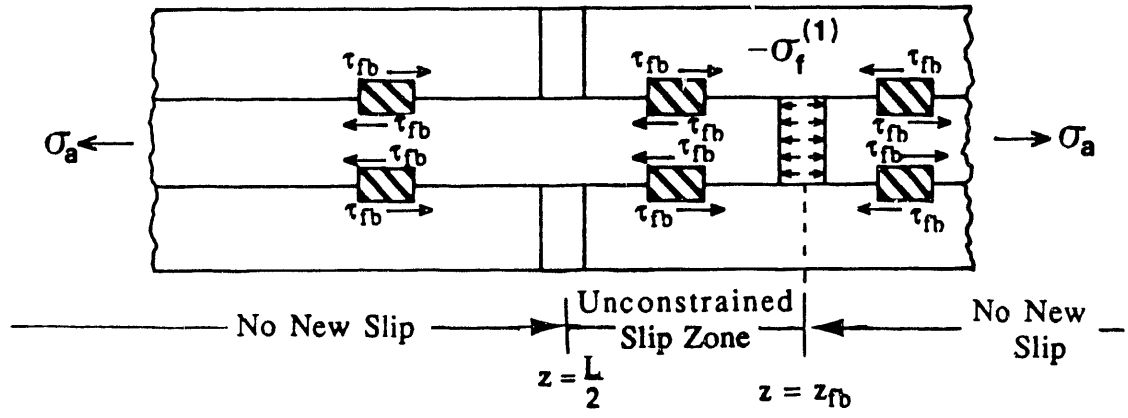

Fig. 6.1. A sketch of the pull-out mechanism when a matrix crack at $z = L/2$ is followed by a fiber break at $z = z_{fb}$.

Employing Eqs. (47) and (48), together with mathematical induction, yields the following expression for the probability of failure within the $2N$ slip zones, each of length l_s, that exist along the specimen of length NL:

$$P_{fs} = P_f \exp\left\{-2\pi a \int_0^{L/2-l_s} \left[\frac{\sigma_z(a,z)}{\sigma_0}\right]^M dz\right\} \times \frac{1-\exp\left\{-4\pi a \int_{L/2-l_s}^{L/2} \left[\frac{\sigma_z(a,z)}{\sigma_0}\right]^M dz\right\}}{1-\exp\left\{-4\pi a \int_0^{L/2} \left[\frac{\sigma_z(a,z)}{\sigma_0}\right]^M dz\right\}} , \quad (49)$$

with P_f given in Eq. (45).

In the derivation of expression (49), we utilized the periodicity of the σ_z^f, namely, $\sigma_z^f\ (a, z + kL) = \sigma_z^f\ (a, z)$ $(k = \pm 1, \pm 2, \ldots)$. For $\tau_s = 0.02$ GPa and $\tau_s = 0.002$ GPa, P_{fs} is indistinguishable from P_f, hence P_{fs} vs σ_a are the same as shown in Fig. 5.1.

For $\tau_s = 0.2$ GPa, P_{fs} differs from P_f. These failure probabilities are shown vs σ_a in Fig. 6.2. Inspection of Figs. 4.2, 5.1, and 6.2 suggests that for $\tau_s = 0.02$ GPa and $\tau_s = 0.002$ GPa, the

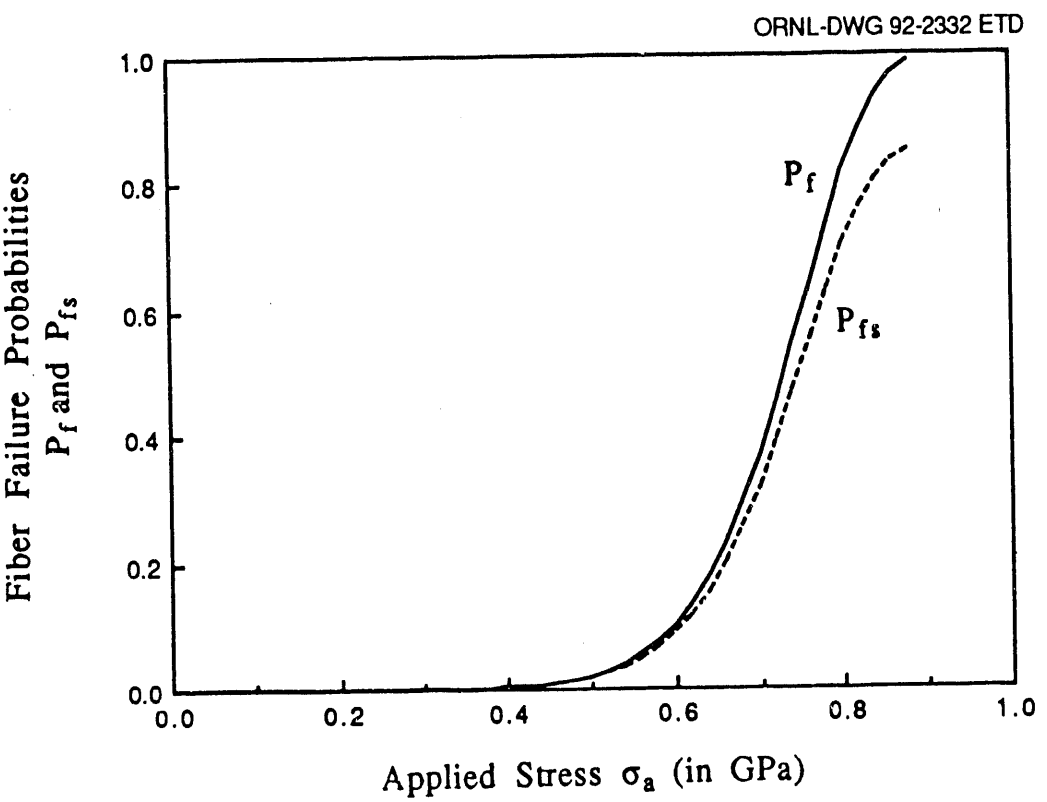

Fig. 6.2. A comparison between P_f, the probability of fiber failure (solid line), and P_{fs}, the probability of fiber failure within a slip zone (dashed line), vs the applied stress σ_a. Case of $\tau_s = 0.2$ GPa and $\alpha_m = \alpha_f$.

incidence of matrix cracking antedates fiber failures, confirming the scenario illustrated in Fig. 6.1. However, for the case of strong interface, that is, τ_s = 0.2 GPa, fiber failures precede matrix cracking.

Employing Eq. (47), we obtain the probability of fiber failure within a single slip zone of a single RVE:

$$P_f\left(\frac{L}{2}-l_s,\frac{L}{2}\right)=\exp\left\{-2\pi a\int_0^{L/2-l_s}\left[\frac{\sigma_z^f(a,z)}{\sigma_0}\right]^M dz\right\}\left(1-\exp\left\{-2\pi a\int_{L/2-l_s}^{L/2}\left[\frac{\sigma_z^f(a,z)}{\sigma_0}\right]^M dz\right\}\right). \quad (50)$$

The most likely location z_{fb}^* of a fiber break within the above slip zones can be evaluated as follows:

$$z_{fb}^*\int_0^{\sigma_a}\int_{L/2-l_s}^{L/2}\frac{\partial^2 P_f(L/2-l_s,z)}{\partial z\,\partial\sigma_a}dz\,d\sigma_a=\int_0^{\sigma_a}\int_{L/2-l_s}^{L/2}\frac{\partial^2 P_f(L/2-l_s,z)}{\partial z\,\partial\sigma_a}z\,dz\,d\sigma_a \quad . \quad (51)$$

Integration by parts yields

$$z_{fb}^*P_f\left(\frac{L}{2}-l_s,\frac{L}{2}\right)=P_f\left(\frac{L}{2}-l_s,\frac{L}{2}\right)\frac{L}{2}-\int_{L/2-l_s}^{L/2}P_f\left(\frac{L}{2}-l_s,z\right)dz \quad . \quad (52)$$

Upon determining z_{fb}^*, it is possible to evaluate U_p, the portion of the pull-out energy resulting from the unresisted contraction of the fiber in the region $z_{fb}^* < z < L/2$. We have

$$U_p=\frac{P_f(L/2-l_s,L/2)}{2E_f}\int_{L/2-z_{fb}^*}^{L/2}\int_0^a\left\{\left[\sigma_z^f(r,z)\right]^2-\left[\sigma_z^f(r,z)-\sigma_z^f(r,z_{fb}^*)\right]^2\right\}r\,dr\,dz \quad . \quad (53)$$

In the evaluation of U_p, we accounted only for the release of σ_z^f due to the creation of a fiber crack at $z = z_{fb}^*$. The contributions to all other stress components have been discarded in view of their relative insignificance.

The nondimensionalized values of $U_p/\pi\,(b^2-a^2)\mathcal{J}_m^c$ vs σ_a are plotted in Fig. 6.3 for τ_s = 0.002, 0.02, and 0.2 GPa. Note the vast disparities between the magnitudes of U_p for these distinct values of τ_s. (The plots for U_p were terminated at P_f = 1.)

It is important to note that when a matrix crack at $z = L/2$ is accompanied by a fiber break at z_{fb}^* within the slip zone, the RVE can no longer support the remote load $\pi b^2\sigma_a$. The unbalanced load of magnitude

$$\pi b^2\sigma_a-P_f\left(\frac{L}{2}-l_s,\frac{L}{2}\right)\int_0^a\sigma_z^f\left(r,z_{fb}^*\right)r\,dr \quad (54)$$

is transferred to the neighboring RVEs by shear at $r = b$. The above unbalanced load will overburden the neighboring RVEs and may bring about their premature failure. This process may explain the observed clustering of failures in the form of fiber pull-outs. However, the local failure of the RVE, accompanied by the overloading of its neighboring elements, leads us beyond the scope of the present model and requires a separate analytical approach.

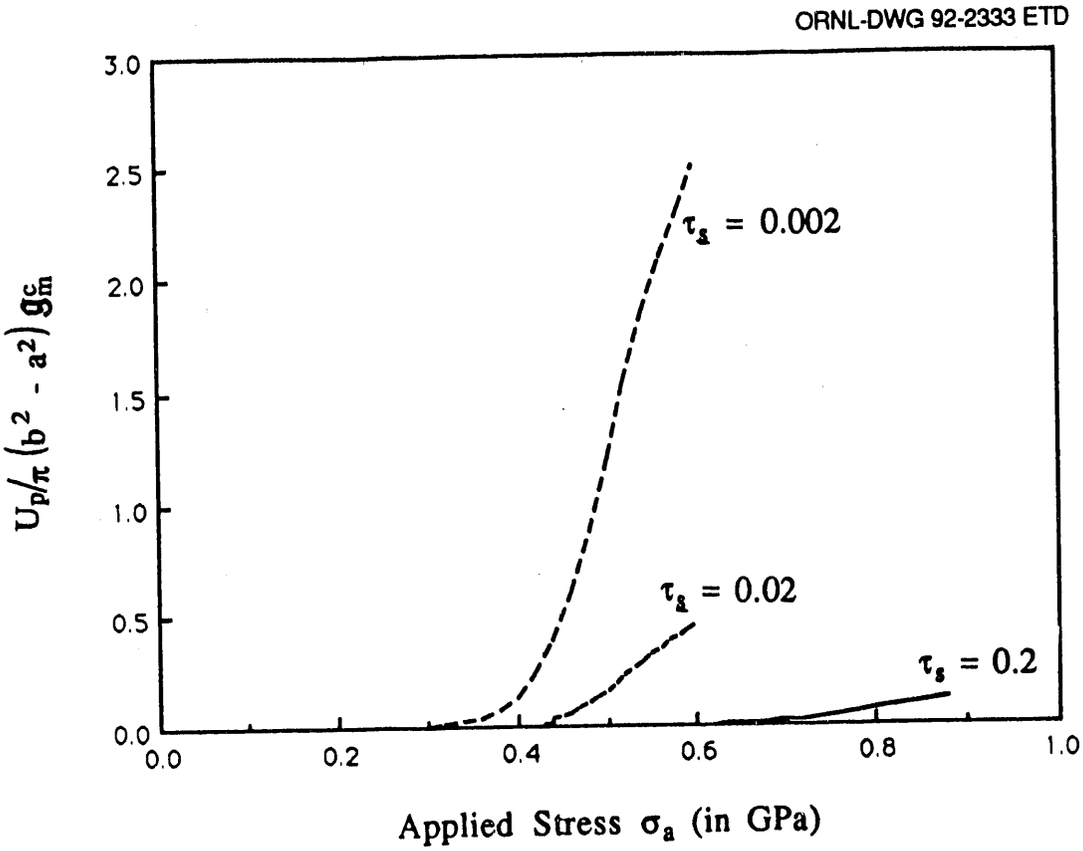

Fig. 6.3. The portion of pull-out energy U_p [Eq. (53)], nondimensionalized by matrix fracture energy, vs the applied stress, σ_a, for several values of interfacial shear strength, τ_s, (in GPa). Case of $\alpha_f = \alpha_m$. All plots were terminated at $P_f = 1.0$.

7. CONCLUSIONS

The results presented in this work illuminate some aspects of the complex response of fiber-reinforced ceramic composites. Figures 4.2 through 4.5 exhibit the effects of various individual parameters, such as the interfacial strength τ_s, the matrix fracture toughness $\mathcal{G}_m^c$, and the thermal mismatch $(\alpha_m - \alpha_f)$, on the stress-strain response of the composite as attributed to progressive matrix cracking alone.

The failure of fibers is predicted by means of Weibull statistics; Figs. 5.1 and 5.2 show the relations between fiber failure probabilities, under monotonically increasing load, and some of the above-mentioned material parameters. The high sensitivity of the latter probabilities to radial distributions of fiber stresses is shown in Figs. 5.3a and 5.3b. This sensitivity is amplified because the "Weibull modulus" M for ceramic fibers has rather high values, namely $8 < M < 10$. As can be noted from Figs. 5.1 to 5.3, the probabilities of fiber failure remain very small at low load level and take sharp upswings in the neighborhoods of some characteristic loads. It was found that the conditional probability of fiber failures to occur within any of the slip zones near the matrix cracks does not differ substantially from the probability of fiber failure anywhere along its length. Consequently, in all realistic cases, the phenomenon of fiber pull-out can be associated with fiber failures taking place within the slip zones. A certain portion of the irreversible fiber-fracture energy, U_p, which is surmised to be the major part of the energy dissipated within an RVE due to fiber break, is exhibited in Fig. 6.3 vs the externally applied stress σ_a for various values of τ_s. It is seen that U_p is much larger for weak interfaces than for strong interfaces. However, the combination of matrix crack and a fiber failure within the adjacent slip zone brings about the local failure of the RVE and the overloading of neighboring fibers. This transfer of load beyond the region of a single RVE requires a separate analysis.

It would seem from Fig. 4.2 that an increase in the interfacial strength τ_s may lead to a better composite. However, such an inference is contradicted by the results shown in Figs. 5.1 and 6.3. When Figs. 4.2, 5.1, and 6.3 are viewed together, it can be seen that fiber strengths are likely to be exhausted before matrix cracking at higher values of τ_s and material failure would occur in a brittle manner. On the other hand, sufficiently low levels of τ_s will give rise to matrix cracks, fiber failures, and fiber pull-outs, resulting in departures from linear stress-strain behavior before ultimate failure.

Finally, bear in mind that at elevated temperatures detrimental effects of oxidation may bring about a brittle-like response of the ceramic composite. As can be seen from Figs. 4.7 and 4.8, smaller values of τ_s cause a larger profusion of matrix cracks, which expose the composite to faster oxidation. This factor must be considered when selecting a specific interfacial strength among several available options.

8. REFERENCES

Aveston, J., Cooper, G.A., and Kelly, A. November 1971. "Single and Multiple Fracture," pp. 15–26 in *The Properties of Fibre Composites*, Conference Proceedings, National Physical Laboratory, IPC Science and Technology Press Ltd.

Bogy, D.B. 1968. "Edge-Bonded Dissimilar Orthogonal Elastic Wedges Under Normal and Shear Loading," *J. Appl. Mech.* **35**, 460.

Budiansky, B., Hutchinson, J.W., and Evans, A.G. 1986. "Matrix Fracture in Fiber-Reinforced Ceramics," *J. Mech. Phys. Solids* **34** (2), 167–189.

Daniel, I.M., Anastassopoulos, G., and Lee, J.-W. 1989. "Experimental Micromechanics of Brittle-Matrix Composites," pp. 133–146 in *Micromechanics: Experimental Techniques*, ed. W.N. Sharpe, Jr., ASME Publication AMD, **102**.

Dollar, A., and Steif, P. S. 1988. "Load Transfer in Composites with a Coulomb Friction Interface," *Int. J. Solids Struct.* **24** (8), 789–803.

Dollar, A., and Steif, P. S. June 1989. "A Tension Crack Impinging Upon Frictional Interfaces," *J. Appl. Mech.* **56**, 291–298.

Evans, A.G. 1990. "Perspective on the Development of High-Toughness Ceramics," *J. Am. Ceram. Soc.* **73** (2), 187–206.

Fang, G.P., Schapery, R.A., and Weitsman, Y. 1989. "Thermally-Induced Fracture in Composites," *Eng. Fract. Mech.* **33** (4), 619–632.

Hillig, W.B. 1987. "Strength and Toughness of Ceramic Matrix Composites," *Am. Rev. Mater. Sci.* **17**, 341–383.

Hutchinson, J.W., and Jensen, H.M. 1990. "Models of Fiber Debonding and Pullout in Brittle Composites with Friction," *Mech. Mater.* **9**, Elsevier, 139–163.

Kelly, A., and Macmillan, N.H. 1986. *Strong Solids*, 3rd ed., Clarendon Press, Oxford, pp. 278.

Kimber, A.C., and Keer, J.G. 1982. "On the Theoretical Average Crack Spacing in Brittle Matrix Composites Containing Continuous Aligned Fibres," *J. Mater. Sci. Lett.* **1**, 353–354.

McCartney, L.N. 1989. "New Theoretical Model of Stress Transfer Between Fibre and Matrix in a Uniaxially Fibre-Reinforced Composite," pp. 215–244 in *Proceedings of the Royal Society of London*, Series A 425.

Nardone, V.C., and Prewo, K.M. 1988. "Tensile Performance of Carbon-Fibre-Reinforced Glass," *J. Mater. Sci.* **23**, 168–180.

Nuismer, R.J., and Tan, S.C. 1988. "Constitutive Relations of a Cracked Composite Lamina," *J. Compos. Mater.* **22**, 306–340.

Schioler, L.J., and Stiglich, J.J., Jr. 1986. "Ceramic Matrix Composites: A Literature Review," *Ceram. Bull.* **65**(2), 289–292.

Schwietert, H.R., and Steif, P.S. 1990. "A Theory for the Ultimate Strength of a Brittle-Matrix Composite," *J. Mech. Phys. Solids* **38**(3), 325–343.

Steif, P.S., and Dollar, A. 1988. "Longitudinal Shearing of a Weakly Bonded Fiber Composite," *J. Appl. Mech.* **55**, 618–623.

Sutcu, M. 1989. "Weibull Statistics Applied to Fiber Failure in Ceramic Composites and Work of Fracture," *Acta Metall.* **37**(2), 651–661.

Tan, S.C., and Nuismer, R.J. 1989. "A Theory for Progressive Matrix Cracking in Composite Laminates," *J. Compos. Mater.* **23**, 1029–1047.

Thouless, M.D., and Evans, A.G. 1988. "Effects of Pull-Out on the Mechanical Properties of Ceramic-Matrix Composites," *Acta Metall.* **36**(3), 517–522.

Timoshenko, S., and Goodier, J.N. 1951. *Theory of Elasticity*, 2nd ed., McGraw-Hill Book Co., Inc., New York, 67.

Washizu, K. 1975. *Variational Methods in Elasticity and Plasticity*, 2nd ed., Pergamon Press, 27–29.

Wijeyewickrema, A.C., et al. 1990. "The Annular Crack Surrounding an Elastic Fiber in a Tension Field," *Int. J. Solids Struct.* (to be published).

APPENDIX A

FORMULATION OF IN-PLANE FIELDS

Consider the following kinematically admissible displacements fields expressed in cylindrical coordinates:

$$\text{In the fiber: } w = \varepsilon_0 z, \quad u = Ar, \quad v = 0; \tag{A.1}$$

$$\text{In the matrix: } w = \varepsilon_0 z, \quad u = Ar + B\left(r - \frac{a}{r}\right), \quad v = 0. \tag{A.2}$$

Consequently, in the fiber:

$$\varepsilon_z^f = \varepsilon_0, \tag{A.3}$$

$$\varepsilon_\theta^f = \varepsilon_r^f = A; \tag{A.4a,b}$$

and in the matrix:

$$\varepsilon_z^m = \varepsilon_0, \tag{A.5}$$

$$\varepsilon_r^m = A + B\left(1 + \frac{a^2}{r^2}\right), \text{ and} \tag{A.6}$$

$$\varepsilon_\theta^m = A + B\left(1 - \frac{a^2}{r^2}\right), \tag{A.7}$$

where A, B, and ε_0 are constants.

By the Hooke's law, the axial stresses in the fiber and the matrix are

$$\sigma_z^f(r,z) = \frac{E_f(1-\nu_f)\varepsilon_0}{(1+\nu_f)(1-2\nu_f)} + \frac{2E_f\nu_f A}{(1+\nu_f)(1-2\nu_f)} - \frac{E_f}{(1-2\nu_f)}\,\varepsilon^{f,th}, \tag{A.8}$$

$$\sigma_z^m(r,z) = \frac{E_m(1-\nu_m)\varepsilon_0}{(1+\nu_m)(1-2\nu_m)} + \frac{2E_m\nu_m(A+B)}{(1+\nu_m)(1-2\nu_m)} - \frac{E_m}{(1-2\nu_m)}\,\varepsilon^{m,th}, \tag{A.9}$$

where

$$\varepsilon^{f,th} = \alpha_f T \quad \text{and} \quad \varepsilon^{m,th} = \alpha_m T. \tag{A.10a,b}$$

The force balance along z-direction provides

$$\sigma_a = \varepsilon_0 E_c + \left(V_f E_f^* \frac{2\nu_f}{1-\nu_f} + V_m E_m^* \frac{2\nu_m}{1-\nu_m} \right) A + V_m E_m^* \frac{2\nu_m B}{1-\nu_m}$$

$$- \frac{1+\nu_f}{1-\nu_f} V_f E_f^* \varepsilon^{f,th} - \frac{1+\nu_m}{1-\nu_m} V_m E_m^* \varepsilon^{m,th} \quad , \tag{A.11}$$

where

$$E_c = V_f E_f^* + V_m E_m^* \quad , \tag{A.12}$$

$$E_f^* = \frac{E_f(1-\nu_f)}{(1+\nu_f)(1-2\nu_f)} \quad , \tag{A.13}$$

$$E_m^* = \frac{E_m(1-\nu_m)}{(1+\nu_m)(1-2\nu_m)} \quad . \tag{A.14}$$

It follows that ε_0 in Eq. (A.11) is given by

$$\varepsilon_0 = \left[\sigma_a - \left(V_f E_f^* \frac{2\nu_f}{1-\nu_f} + V_m E_m^* \frac{2\nu_m}{1-\nu_m} \right) A - V_m E_m^* \frac{2\nu_m B}{1-\nu_m} \right.$$

$$\left. + \frac{1+\nu_f}{1-\nu_f} V_f E_f^* \varepsilon^{f,th} + \frac{1+\nu_m}{1-\nu_m} V_m E_m^* \varepsilon^{m,th} \right] \Big/ E_c \quad . \tag{A.15}$$

Turning to the radial stresses σ_r in the fiber and matrix, we have

$$\sigma_r^f = \frac{E_f^*}{1-\nu_f} A + \frac{E_f^* \nu_f}{1-\nu_f} \varepsilon_0 - \frac{1+\nu_f}{1-\nu_f} E_f^* \varepsilon^{f,th} \tag{A.16}$$

and

$$\sigma_r^m = \frac{E_m^*}{1-\nu_m}(A+B) + \frac{E_m^*(1-2\nu_m)a^2 B}{(1-\nu_m)r^2} + \frac{E_m^* \nu_m}{1-\nu_m} \varepsilon_0 - \frac{1+\nu_m}{1-\nu_m} E_m^* \varepsilon^{m,th} \quad . \tag{A.17}$$

The continuity condition $\sigma_r^f = \sigma_r^m$ at $r = a$ and the boundary condition $\sigma_r^m = 0$ at $r = b$ yield the following equations for the unknowns A and B:

$$C_{11} A + C_{12} B = f_1 \quad , \tag{A.18a}$$

$$C_{21}A + C_{22}B = f_2 \quad , \tag{A.18b}$$

where

$$C_{11} = 1 - \left(V_f E_f^* \frac{2\nu_f}{1-\nu_f} + V_m E_m^* \frac{2\nu_m}{1-\nu_m} \right) \frac{\nu_m}{E_c} \quad , \tag{A.19a}$$

$$C_{12} = 1 + V_f(1-2\nu_m) - \frac{2\nu m^2 V_m E_m^*}{(1-\nu_m)E_c} \quad , \tag{A.19b}$$

$$\begin{aligned} C_{21} = & \left[1 - \left(V_f E_f^* \frac{2\nu_f}{1-\nu_f} + V_m E_m^* \frac{2\nu_m}{1-\nu_m} \right) \frac{\nu_f}{E_c} \right] \frac{E_f^*}{1-\nu_f} \\ & - \left[1 - \left(V_f E_f^* \frac{2\nu_f}{1-\nu_f} + V_m E_m^* \frac{2\nu_m}{1-\nu_m} \right) \frac{\nu_m}{E_c} \right] \frac{E_m^*}{1-\nu_m} \quad , \end{aligned} \tag{A.19c}$$

$$C_{22} = \frac{\nu_m V_m E_m^*}{(1-\nu_m)E_c} \left(\frac{E_m^* \nu_m}{1-\nu_m} - \frac{E_f^* \nu_f}{1-\nu_f} \right) - 2E_m^* \quad , \tag{A.19d}$$

$$f_1 = -\frac{\nu_m \sigma_a}{E_c} + (1+\nu_m)\varepsilon^{m,th} - \frac{\nu_m}{E_c} \left(\frac{1+\nu_f}{1-\nu_f} V_f E_f^* \varepsilon^{f,th} + \frac{1+\nu_m}{1-\nu_m} V_m E_m^* \varepsilon^{m,th} \right) \quad , \tag{A.20a}$$

$$\begin{aligned} f_2 = & \frac{1+\nu_f}{1-\nu_f} E_f^* \varepsilon^{f,th} - \frac{1+\nu_m}{1-\nu_m} E_m^* \varepsilon^{m,th} \\ & + \left[\frac{\nu_m E_m^*}{(1-\nu_m)E_c} - \frac{\nu_f E_f^*}{(1-\nu_f)E_c} \right] \left(\sigma_a + \frac{1+\nu_f}{1-\nu_f} V_f E_f^* \varepsilon^{f,th} + \frac{1+\nu_m}{1-\nu_m} V_m E_m^* \varepsilon^{m,th} \right) \quad . \end{aligned} \tag{A.20b}$$

In addition, it may be noted from Eqs. (A.18) to (A.20) that A and B depend linearly on σ_a, $\varepsilon^{f,th}$, and $\varepsilon^{m,th}$, namely

$$A\left(\sigma_a, \varepsilon^{f,th}, \varepsilon^{m,th}\right) = \sigma_a A_1 + \varepsilon^{f,th} A_2 + \varepsilon^{m,th} A_3 \quad , \tag{A.21a}$$

with

$$A_1 = O(\nu_m) + O(\nu_f) \tag{A.21b}$$

and

$$B\left(\sigma_a, \varepsilon^{f,th}, \varepsilon^{m,th}\right) = \sigma_a B_1 + \varepsilon^{f,th} B_2 + \varepsilon^{m,th} B_3 \quad , \tag{A.22a}$$

with

$$B_1 = O(v_m) + O(v_f) \quad . \tag{A.22b}$$

Consequently, it can be concluded that contribution to σ_z^f in Eq. (A.8) and σ_z^m in Eq. (A.9) from the mechanical part of the transverse strains is of $O(v_m^2)$, $O(v_f^2)$, or $O(v_f v_m)$. The small significance of this contribution would mitigate the effects of inaccuracies caused by our employment of boundary conditions (4a) and (4b) in constructing the present model.

APPENDIX B

THE BOUNDARY ELEMENT SCHEME

Consider a two-dimensional representative volume element (RVE) in rectangular Cartesian coordinates as shown in Fig. B.1. The RVE consists of two linear isotropic elastic materials, loaded as shown in the figure. Assume perfect bond to exist at the interfaces $|x| = a$ between the two materials for $|\tau_{xz}| < \tau_s$, and let slip occur when $|\tau_{xz}| = \tau_s$ at those interfaces. Denote by l_s the length of the slip zone.

The continuity of displacement and stress components at the nonslip interface $0 \le z \le L/2 - l_s$ is expressed by

$$\tau_{xz}^f = \tau_{xz}^m \ , \quad \sigma_x^f = \sigma_x^m \ , \quad u_x^f = u_x^m \ , \quad \text{and } u_z^f = u_z^m \ . \tag{B.1}$$

While at the slip interface $L/2 - l_s \le z \le L/2$, the mechanical conditions are given by

$$\tau_{xz}^f = -\tau_s \ , \quad \tau_{xz}^m = -\tau_s \ , \quad \sigma_x^f = \sigma_x^m \ , \quad \text{and } u_x^f = u_x^m \ . \tag{B.2}$$

In addition, the continuity of τ_{xz} at the interface imposed the following relation

$$\tau_{xz}(z, x = a) = -\tau_s \ , \tag{B.3}$$

as z approaches $L/2 - l_s$ from the nonslip side.

The boundary element method was employed to solve for the stress and displacement fields. The resulting stress components σ_z^f were plotted vs x at several levels of z in Fig. B.2.

Notice that the value of l_s is unknown a priori. Therefore, a guess initial value of l_s is first introduced into the boundary element method algorithm, leading to a certain solution which, in general, does not match the requirement (B.3). This value of l_s was then adjusted iteratively, with corresonding values of l_s, until Eq. (B.3) was satisfied to within a desired accuracy.

For comparison, Fig. B.2 also contains plots of the values of σ_z^f computed by the method developed in this paper for the concentric cylindrical model shown in Fig. 2.1. Equivalent elastic properties, geometrical parameters, and loading conditions were employed for both cases shown in Fig. B.2.

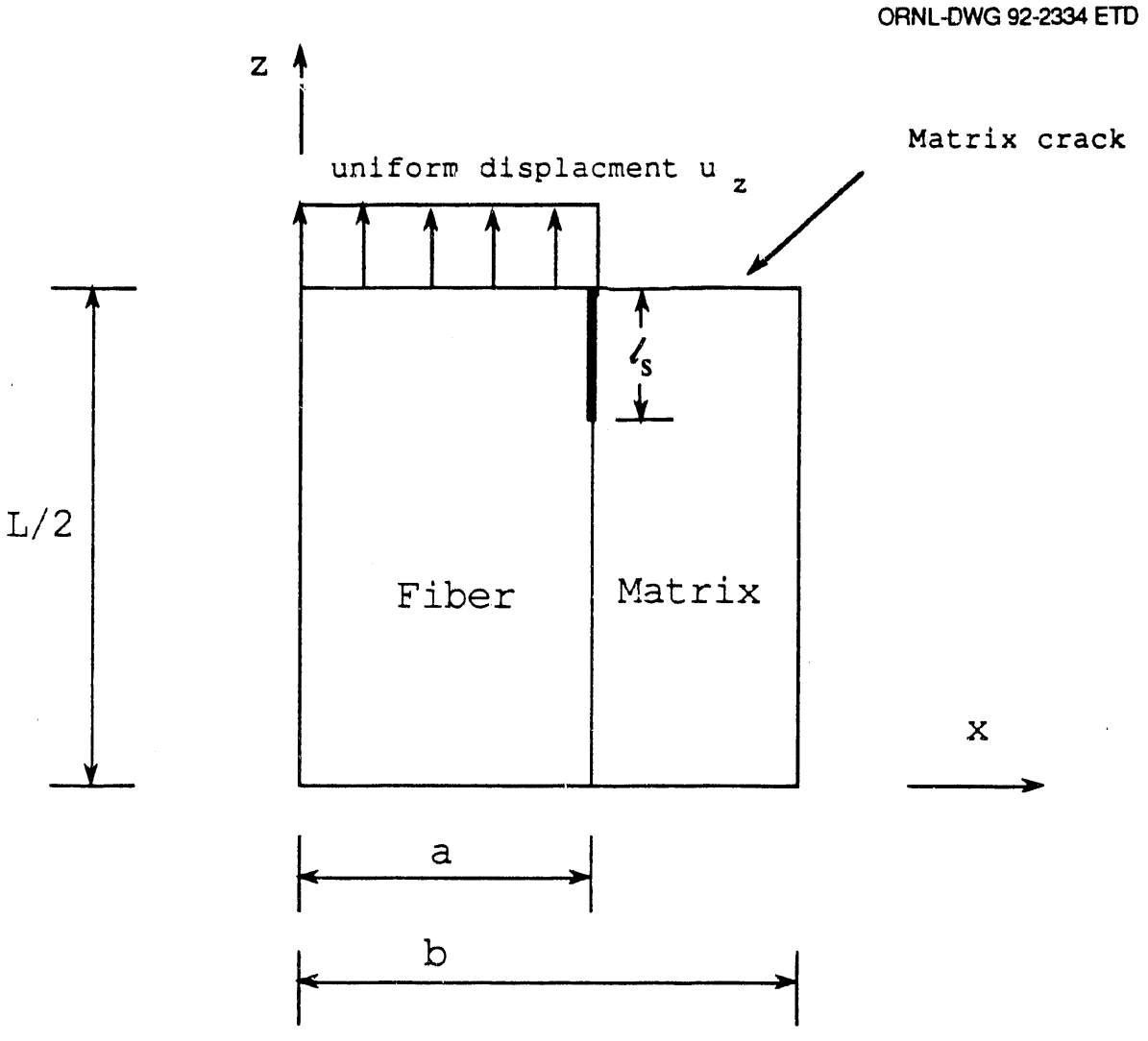

Fig. B.1. The Cartesian configuration employed for the boundary element method. The computations employed $L/a = 8$, $a/b = 0.4$.

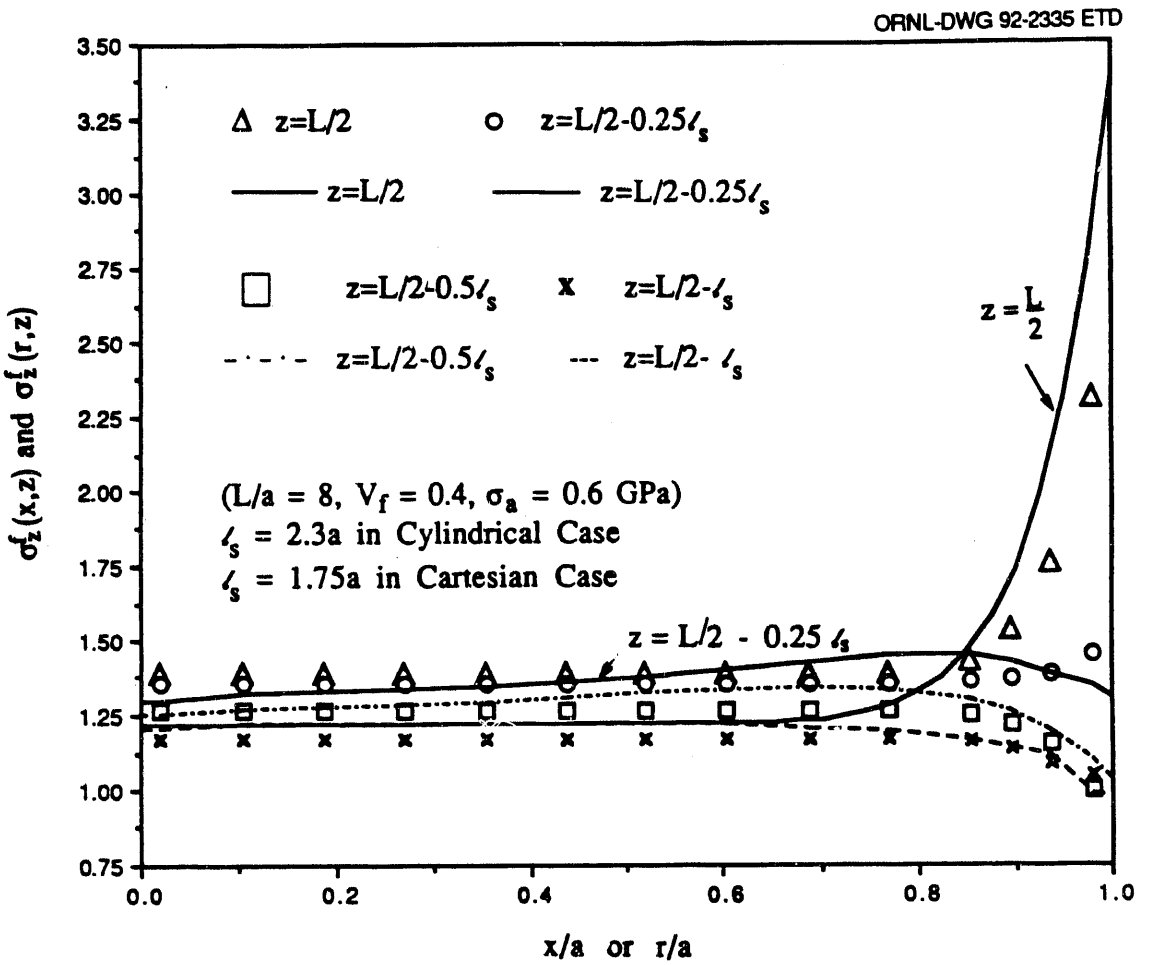

Fig. B.2. Profiles of fiber stresses σ_z^f (x, z) vs x/a computed by the boundary element method (discrete points) compared with σ_z^f (r, z) vs r/a evaluated by the present model.

Internal Distribution

1. P. F. Becher
2. T. M. Besman
3. H. W. Blake
4. J. J. Blass
5. R. A. Bradley
6. R. D. Cheverton
7. J. A. Clinard
8. J. L. Cook
9. J. M. Corum
10. D. F. Craig
11. R. C. Gwaltney
12. W. R. Hendrich
13. C. Hsueh
14. R. L. Huddleston
15. J. E. Jones Jr.
16. C. R. Luttrell
17. W. R. Martin
18. J. G. Merkle
19. S. E. Moore
20. D. G. O'Connor
21. A. B. Poole
22. C. E. Pugh
23. M. B. Ruggles
24. W. K. Sartory
25. J. T. Shaffer
26. F. W. Swinson
27. B. B. Thomas
28. D. A. Waters

29–43. Y. J. Weitsman

44. E. W. Whitfield
45. G. T. Yahr
46. A. Zucker
47. ORNL Patent Section
48. Central Research Library
49. Document Reference Section

50–51. Laboratory Records Department

52. Laboratory Records (RC)

External Distribution

53. J. A. Boulet, Dept. of Engineering Science and Mechanics, Rm. 310, Perkins Hall, The University of Tennessee, Knoxville, TN 37996-2030
54. T. G. Carley, Dept. of Engineering Science and Mechanics, Rm. 310, Perkins Hall, The University of Tennessee, Knoxville, TN 37996-2030
55. R. D. Krieg, Dept. of Engineering Science and Mechanics, Rm. 310, Perkins Hall, The University of Tennessee, Knoxville, TN 37996-2030
56. J. D. Landes, Dept. of Engineering Science and Mechanics, Rm. 310, Perkins Hall, The University of Tennessee, Knoxville, TN 37996-2030
57. M. Madhukar, Dept. of Engineering Science and Mechanics, Rm. 310, Perkins Hall, The University of Tennessee, Knoxville, TN 37996-2030
58. J. E. Stoneking, Dept. of Engineering Science and Mechanics, Rm. 310, Perkins Hall, The University of Tennessee, Knoxville, TN 37996-2030

59–61. H. Zhu, Dept. of Engineering Science and Mechanics, Rm. 310, Perkins Hall, The University of Tennessee, Knoxville, TN 37996-2030

62. J. D. Achenbach, Northwestern University, Catalysis Bldg., 2137 N Sheridan Rd., Evanston, IL 60208
63. D. Allen, Director, Ctr. for Mech. of Comp., Aer. Eng. Dept., Texas A&M University, Room 736D—HR Bright Bldg., College Station, TX 77843-3141
64. G. L Anderson, Chief, Struct. and Dynamics Branch, Engineering Sciences Div., U.S. Army Research Office, P.O. Box 12211, Research Triangle Park, NC 27709-2211
65. Professeur Agrege, Didier Baptiste, Ecole Centrale Paris, Grande Voie des Vignes, 92295 Chatenay-Malabry cedex
66. S. N. Atluri, Georgia Institute of Technology, School of Eng. and Mech., Atlanta, GA 30332
67. Jonathon Awerbuch, Drexel University, Mechnical Engineering Department, Philadelphia, PA 19104

68. B. Budiansky, Division of Applied Sciences, Harvard University, Cambridge, MA 02138
69. C. C. Chamis, National Aeronautics and Space Administration, Lewis Research Center, Cleveland OH 44135
70. F. P. Chiang, State University of New York, Department of Mechanical Engineering, Stony Brook, NY 11794
71. Tsu-Wei Chou, University of Delaware, Department of Mechanical Engineering, Newark, DE 19711
72. Francois Christin, Mat. Devt. Mgr., Comp. Operations, Societe Europenne de Propulsion, Solid Propulsion and Composites Division, Le Haillan B.P. 37, 33165 St. Medard en Jalles France
73. R. M. Christensen, Fiber Composites and Mechanics, Lawrence Livermore National Laboratory, L-338, University of California, P.O. Box 808, Livermore, CA 94550
74. I. M. Daniel, Robert R. McCormick School of Engineering and Applied Sciences, Northwestern University, Evanston, IL 60208
75. F. Delale, Dept. of Mechnical Engineering, The City College, Convent Ave. at 183th St., New York, NY 10031
76. D. C. Drucker, Division of Engineering Sciences and Mechanics, University of Florida, Gainesville, FL 32611
77. G. J. Dvorak, Head, Civil Engineering Department, Rensselaer Polytechnic Institute, Troy, NY 12181
78. W. W. Feng, Lawrence Livermore National Laboratory, L-342, Livermore, CA 94550
79. L. B. Freund, Division of Engineering, Brown University, Providence, RI 02912
80. R. H. Gallagher, University of Arizona, Dean of Engineering, Tucson, AZ 85721
81. J. G. Goree, Clemson University, 320 Riggs Hall, Clemson, SC 29634-0921
82. Tom Hahn, Department of Engineering Sciences and Mechanics, Pennsylvania State University, 227 Hammond Bldg., University Park, PA 16802
83. P. G. Hodge, Jr., Department of Aerospace Engineering and Mechanics, University of Minnesota, Minneapolis, MN 55455
84. W. F. Jones, Program Manager, Directorate of Aero. Sciences, AFOSR/NA, Boling Air Force Base. Washington, DC 20332-6448
85. Nils Juhlin, VP, NovaComp Eng., Inc., P.O. Box 95137, Seattle, WA 98145-2137
86. M. F. Kanninen, Southwest Research Institute, P.O. Drawer 28510, 6220 Culebra Rd., San Antonio, TX 78284
87. Keith Kedward, University of California, Department of Mechinical Engineering, Santa Barbara, CA 93106
88. Prof. Kinra, Mech. and Mat. Eng., Texas A&M University, College Station, TX 77843
89. A. S. Kobayashi, Department of Mechanical Engineering, University of Washington, Seattle, WA 98195
90. Dusan Krajcinovic, Department of Mech. and Aero. Eng., Arizona State University, Tempe, AZ 85287-6106
91. F. A. Leckie, Head, Department of Mechanical Engineering, University of California, Santa Barbara, Santa Barbara, CA 93106
92. Norman Laws, Department of Mechnical Engineering, University of Pittsburgh, Pittsburgh, PA 15260
93. Harold Liebowitz, Dean, School of Eng. and Appl. Sci., George Washington University, Washington, DC 20052
94. L. N. McCartney, National Physical Laboratory, Div. of Materials Metrology, Bldg. 13, Teddington, Middlesix TW11 0LW, England
95. F. A. McClintock, Department of Mechanical Engineering, Massachusetts Institute of Technology, Cambridge, MA 02139
96. Hidenori Murakami, University of California, Department of AMES, B-010, LaJolla, CA 92093
97. Seiichi Nomura, Assoc. Prof. of Mechanical Engineering, The University of Texas, Box 19023, Arlington, TX 76019-0023
98. Ralph Nuismer, Hercules Corporation, P.O. Box 98, Magna, UT 84044

99. Nicholas Pagano, Wright Laboratory MLBM, Wright Patterson Air Force Base, OH 45433
100. D. M. Parks, Massachusetts Institute of Technology, Department of Mech. Eng., Cambridge, MA 02139
101. Lee Phoenix, Sibley School of Mech. and Aero. Eng., Cornell University, Grumman and Upson Halls, Ithaca, NY 14853-7501
102. Daniel Post, Virginia Ploytechnic Institute, Dept. of Eng. Sci. and Mech., Blacksburg, VA 24061
103. Ryszard Pyrz, Aalborg University, Inst. of Mech. Eng., Pontoppidanstrabe 101, DK-9220 Aalborg, Denmark
104. F. G. Rammerstorfer, Christian Doppler Lab., Micromech of Materials, Gusshausstrasse 27-29, A-1040 Vienna, Austria
105. J. N. Reddy, Virginia Polytechnic Institute, Dept. of Eng. Sci. and Mech., 220 Norris Hall, Blacksburg, VA 24061
106. K. L. Reifsnider, Virginia Polytechnic Institute, Dept. of Eng. Sci. and Mech., Blacksburg, VA 24061
107. J. R. Rice, Harvard University, Div. of Appl. Sci., Cambridge, MA 02138
108. J. Rose, Drexel University, Dept. of Mech. Eng. and Mech., Philadelphia, PA 19104
109. A. A. Rubinstein, Tulane University, Dept. of Mech. Eng., New Orleans, LA 70118
110. J. L. Sanders, Harvard University, Div. of Appl. Sci., Cambridge, MA 02138
111. M. H. Santare, University of Delaware, Newark, DE 19716
112. R. A. Schapery, Aerospace Eng. and Eng. Mech., University of Texas, Austin, TX 78712-1085
113. G. C. M. Sih, LeHigh University, Inst. of Fracture and Solid Mechanics, Bethlehem, PA 18015
114. M. G. Simpson, Sr. Process Engineer, 3M Delta G, 9960-A Glenoaks Blvd., Sun Valley, CA 91352
115. Patrick Spriet, Applications Development Mgr., SEP, Inc., 1100 17th St. NW Suite 320, Washington, DC 20036
116. J. H. Starnes, Jr., NASA Langley Research Center, 8 W Taylor Rd., MS 190, Hampton, VA 23665
117. W. S. Steffier, Prog. Mgr., Ceramic-Matrix Composites, BP Chemicals Eng. Systems, 13722 Harvard Pl, Gardena, CA 90249-2529
118. C. T. Sun, Dept. of Aero. and Astro., Purdue University, Rm. 331, Grissom Hall, Lafayette, IN 47907
119. S. R. Swanson, Dept. of Mech. and Ind. Eng., University of Utah, Salt Lake City, UT 84112
120. Ramesh Talreja, Georgia Institute of Technology, School of Aero. Eng., Atlanta, GA 30332-0150
121. M. Taya, Dept. of Mechanical Engineering, University of Washington, Seattle, WA 98195
122. Prof. Walton, Dept. of Mech. Eng., Texas A&M University, College Station, TX 77843
123. Albert Wang, Mech. Eng. Dept., Drexel University, Philadelphia, PA 19104
124. Su Su Wang, Dept. of Mech. Eng., University of Houston, 4800 Calhoun Rd., Houston, TX 77204-4792
125. J. B. Whiteside, Head, Applied Mechanics, Research Department, Grumman Aerospace Corp., MS A08-35, Bethpage, NY 11714
126. S. W. Yurgartis, Dept. of Mech. and Aero. Eng., Clarkson University, Potsdam, NY 13699-5725
127. Dr. Yevgeny, Eng., Prod. Design and Mech. Div., Alcoa Labs, ALCOA, Alcoa Center, PA 15069
128. Office of Assistant Manager for Energy Research and Development, Department of Energy, OR, Oak Ridge, TN 37831
129–138. Office of Scientific and Technical Information, P.O. Box 62, Oak Ridge, TN 37831

END

DATE
FILMED
4/06/92